

Radio Observations of Discs around Young Stellar Objects

Raeesa Parker

A THESIS SUBMITTED IN PARTIAL FULFILMENT
OF THE REQUIREMENTS FOR THE DEGREE OF
MASTER OF SCIENCE

Jeremiah Horrocks Institute for Maths, Physics and Astronomy
University of Central Lancashire

December 2017

Declaration

The work presented in this thesis was carried out at the Jeremiah Horrocks Institute for Maths, Physics and Astronomy, University of Central Lancashire. This thesis has been submitted in partial fulfilment of the requirements for the degree of Master of Science.

I declare that while registered as a candidate for the research degree, I have not been a registered candidate or enrolled student for another award of the University or other academic or professional institution.

I declare that no material contained in the thesis has been used in any other submission for an academic award. Data and models used in this thesis that are not my own are clearly cited in the text.

I declare that this research program is not part of a collaborative project; nor that a proof-reading service was used in the compilation of this thesis.

I further declare that all work conducted in this thesis is my own original research carried out under the supervision of Professor Derek Ward-Thompson, with the following exceptions:

The observations and data reduction of DG Tau B presented in Chapter 3 were conducted by members of the PEBBLEs team; of which I am a member. Aligning the centres of DG Tau B in both epochs as well as the data analysis is my own original research.

The observations and data reduction of DG Tau B presented in Chapter 4 were conducted by members of the Disks@EVLA team; of which I am not a member.

Permission from the Principle Investigator, Professor Claire Chandler, was sought before analysis of the data began, however, I carried out all of the analysis.

All of the work in Chapter 5 is my own original research unless explicitly stated.

Signed

A rectangular box containing a handwritten signature in black ink. The signature appears to be 'Raeesa Parker' written in a cursive style.

.....

Raeesa Parker

Abstract

In this thesis we study the disc surrounding the Young Stellar Object DG Tau B. We present observations at both cm and mm wavelengths using e-MERLIN and the EVLA respectively. We study the cold dust in the disc of DG Tau B by looking at its spectral energy distribution (SED). We also analyse the proper motions of DG Tau B and the classical T Tauri star DG Tau A to determine if they are a binary.

We fit a modified blackbody to the DG Tau B SED and model the dust using a temperature of $T=9.6\pm 0.6\text{K}$ and a mass of $M=0.30\pm 0.03M_{\odot}$. We see a radio excess which is found to have a spectral index of $\alpha = 1.4 \pm 0.2$, which is indicative of free-free or synchrotron emission.

The emission from DG Tau B at cm wavelengths is studied at two epochs. The jet of DG Tau B is resolved with e-MERLIN in both the 2014 and 2016 data, whilst the disc of DG Tau B is only marginally resolved in 2016. The lack of cm blackbody emission from the DG Tau B disc, and shallow spectral index of the radio excess, may indicate that there are no cm-sized dust grains in the disc of DG Tau B.

However, the disc of DG Tau B is resolved at mm wavelengths whilst the jet is not. This could either be attributed to mm-sized dust grains in the disc of DG Tau B or be an indication of the dust temperature in the disc.

We study the proper motions of DG Tau A and B and find them to be consistent with each other. This could be explained if they have formed from the same star-forming region. Further investigation would need to be conducted in order to confirm if the two Young Stellar Objects are part of a binary system.

Contents

Declaration	i
Abstract	iii
Acknowledgements	xiii
1 Introduction	1
1.1 Formation of Protoplanetary Discs	2
1.2 Planetesimal Formation	5
1.3 Observations of Protoplanetary Discs	7
2 Radio Interferometry and e-MERLIN	12
2.1 Introduction to Radio Interferometry	12
2.2 Calibrating Radio Interferometric Data	17
2.3 e-MERLIN	19
2.4 EVLA	21
3 A cm Study of DG Tau B	23
3.1 Previous Studies of DG Tau B	23
3.2 New data : Observations with e-MERLIN	24
3.3 Spectral Energy Distribution	28
3.4 Cross Cut Analysis	31

4	A mm Study of DG Tau B	40
4.1	New Data : Observations with the EVLA	40
4.2	Cross Cut Analysis	43
5	Discussion	47
5.1	SED Fitting	48
5.2	Comparing the SED Results with Previous Observations	52
5.3	Gaussian Fitting	53
5.3.1	e-MERLIN Cross Cuts	53
5.3.2	Combining Epochs	57
5.3.3	EVLA Cross Cuts	61
5.4	DG Tau B Jet	64
5.5	Is DG Tau A and B A Binary?	66
5.6	Comparing the Proper Motions to Previous Results	70
6	Conclusion and Future Work	76
6.1	SED Fitting	76
6.2	Centimetre Observations of DG Tau B	77
6.3	Millimetre Observations of DG Tau B	78
6.4	The relationship between DG Tau A and B	79
6.5	Future Work	79

List of Tables

2.1	e-MERLIN capabilities in the C band (Garrington et al. 2004)	19
2.2	EVLA capabilities in the Ka band (Perley et al. 2011)	22
3.1	Parameters of DG Tau B found by fitting elliptical Gaussians to the data.	28
3.2	Flux values from previous observations of DG Tau B used in the SED.	29
3.3	Parameters of DG Tau B found by fitting 2D Gaussian models to the two epochs of data. The angle of the major axis is measured anticlockwise from north.	32
3.4	Parameters of the beam in each epoch	35
4.1	Parameters of DG Tau B found by fitting elliptical Gaussians to the EVLA data.	42
4.2	Parameters of DG Tau B found by fitting a 2D Gaussian model to the EVLA data. The angle of the major axis is measured anticlockwise from north.	45
5.1	Positions of DG Tau A used to investigate the proper motion of the system.	67
5.2	Positions of DG Tau B used to investigate the proper motion of the system.	68

5.3	The proper motions of DG Tau A and B derived in this thesis as well as from the literature	74
-----	---	----

List of Figures

1.1	The evolutionary sequence of Young Stellar Objects, including their SED's (Andre 1994).	4
1.2	The different outcomes of particle collisions (Windmark et al. 2012).	7
1.3	Plank's law for temperatures of 5000K, 500K and 50K. The emission at high frequencies is described by Wien's approximation whilst the Rayleigh Jeans law describes the emission at low frequencies.	9
1.4	SED of a protoplanetary disc and the origin of various components. (Dullemond et al. 2007).	10
2.1	The relationship between the image plane and the (u,v) plane is shown here. \bar{s} is a unit vector in the direction of the object. \bar{b} is the baseline length between two telescopes of the array.	13
2.2	The interferometer e-MERLIN consists of seven telescopes situated across England.	20
2.3	The EVLA interferometric array consists of twenty seven telescopes in a Y-shaped configuration. Each telescope is 25 m in diameter. Image from NRAO/AUI.	22

3.1	SMA observations at 1.3mm by Zapata et al. (2015) show the disc of DG Tau B (contour). The peak continuum emission is $0.31 \text{ Jy beam}^{-1}$ and the contours range in steps of 15% from 25% to 85% of the peak emission. SMA ^{12}CO emission of the molecular outflow (red) traces the DG Tau B jet. C1 and C2 indicate where position-velocity measurements were made by Zapata et al. (2015). Observations taken using the HST Wide-Field Planetary Camera 2 conducted by Stapelfeldt et al. (1997) are also shown. Observations were taken at $\approx 800\text{nm}$ (blue) and $\approx 670\text{nm}$ (green).	25
3.2	e-MERLIN Observations of DG Tau B taken in 2014 (top) and 2016 (bottom).	27
3.3	SED of DG Tau B plotted using observations made in this thesis and archive data. A modified blackbody has been fitted to the dust emission from DG Tau B. The dust has been modelled with a temperature of $T=9.6 \pm 0.6\text{K}$ and a mass of $m=0.3 \pm 0.03M_{\odot}$. The radio excess (red) is a combination of free-free emission (blue) and thermal greybody emission (yellow).	33
3.4	Image of DG Tau B made by combining and averaging the data from the 2014 and 2016 epoch. The observations were first aligned by assuming the position of the peak is due to DG Tau B. The 2016 epoch was then rotated to ensure the jet of DG Tau B was aligned in both epochs.	35
3.5	The emission from DG Tau B studied along the major and minor axis of the Gaussian model. The emission has been fit with a Gaussian and is shown in blue; the beam is shown in red. Observations used to make this cross cut were made in 2014.	36

3.6	The emission from DG Tau B studied along the major and minor axis of the Gaussian model. The emission has been fit with a Gaussian and is shown in blue; the beam is shown in red. Observations used to make this cross cut were made in 2016.	37
3.7	The emission from DG Tau B studied along the major and minor axis of the Gaussian model. The emission has been fit with a Gaussian and is shown in blue; the beam is shown in red. This cross cut was made using the combined observations of DG Tau B in 2014 and 2016.	38
4.1	Observation of DG Tau B taken with the EVLA in 2010. The observations were taken at a frequency of 34.0 GHz (8.8 mm). The beam, in the lower left, is $0.08 \times 0.07''$ with a position angle of -73.0°	41
4.2	The emission from DG Tau B studied along the major and minor axis of the Gaussian model. The emission has been fit with a Gaussian and is shown in blue; the beam is shown in red. The beam has dimensions of 80×70 mas. Observations used to make this cross cut were made in 2010 using the EVLA.	46
5.1	The cold dust in this SED of DG Tau B has been fit with the best fit model (black) as well as the upper and lower limit on the disc mass and temperature. The best fit (black) has been modelled with a a mass of $M = 0.30 \pm 0.03 M_\odot$ and temperature of $T = 9.6\text{K}$. The upper limit on the disc mass ($0.53 \pm 0.10 M_\odot$) has been modelled using a temperature of 7K (red). Whilst the lower limit on the disc mass ($0.13 \pm 0.10 M_\odot$) has been derived using a temperature of 17K (blue).	54

5.2	The emission from DG Tau B studied along the major and minor axis of the Gaussian model. The emission has been fit with a Gaussian and is shown in blue; the beam is shown in red. Observations used to make this cross cut were made in 2014. This figure is a replica of Figure 3.5 and has been included for ease of reference.	56
5.3	The emission from DG Tau B studied along the major and minor axis of the Gaussian model. The emission has been fit with a Gaussian and is shown in blue; the beam is shown in red. Observations used to make this cross cut were made in 2016. This figure is a replica of Figure 3.6 and has been included for ease of reference.	58
5.4	The emission from DG Tau B studied along the major and minor axis of the Gaussian model. The emission has been fit with a Gaussian and is shown in blue; the beam is shown in red. This cross cut was made using the combined observations of DG Tau B in 2014 and 2016. This figure is a replica of Figure 3.7 and has been included for ease of reference.	60
5.5	The emission from DG Tau B studied along the major and minor axis of the Gaussian model. The emission has been fit with a Gaussian and is shown in blue; the beam is shown in red. The beam has dimensions of 80×70 mas. Observations used to make this cross cut were made in 2010 using the EVLA. This figure is a replica of Figure 4.2 and has been included for ease of reference.	63
5.6	The right ascension (a) and declination (b) of DG Tau A over a 35 year period. The straight lines are least squares fits to the data that give the proper motions discussed in the text.	69

5.7	The right ascension (a) and declination (b) of DG Tau B over a 22 year period. The straight lines are least squares fits to the data that give the proper motions discussed in the text.	71
5.8	The right ascension (a) and declination (b) of DG Tau B over a 22 year period. The data used to generate these plots does not include the two VLA observations conducted by Rodríguez, Dzib, Loinard, Zapata, Raga, Cantó & Riera (2012) in 2009 and 2011. The straight lines are least squares fits to the data that give the proper motions discussed in the text.	73

Acknowledgements

Firstly, I would like to thank my supervisor, Professor Derek Ward-Thompson, for giving me the opportunity to conduct this research. I would also like to thank him for his amazing guidance and patience, as well as for having read this thesis a number of times. I have learnt a great deal over the past year under the supervision of Professor Derek and look forward to working with him in the future.

I would like to thank all the members of the star formation research group at the Jeremiah Horrocks Institute, particularly Dr. Jason Kirk, Dr. Kate Pattle and Dr. David Bresnahan for their endless good advice and help. I have thoroughly enjoyed our research meetings, where I have not only learnt an immense amount about star formation but also how to become a better researcher.

I would also like to thank Dr Anita Richards (University of Manchester) and Dr. Megan Argo (University of Central Lancashire) for introducing me to the amazing world of radio interferometry as well as how to think in Fourier space. Further thanks to Dr. Jane Greaves and Dr. Emily Drabek-Maunder for providing me with an introduction to the project and data. I look forward to working with them on future projects.

Lastly, I would like to thank my family, for providing endless support throughout this project and without whom I wouldn't have made it this far.

Chapter 1

Introduction

It is now known that the sun is not the only star to harbour planets. The first confirmed exoplanet was detected in 1992 (Wolszczan & Frail 1992) and over three thousand exoplanets have since been discovered. There is a great diversity in the discovered planets, with some being smaller than Mercury, whilst others are almost twice as big as Jupiter. Exoplanets have also been discovered to orbit at radii greater than that of our Solar System, as well as some free-floating planets. Unlike our Solar System, exoplanets have also been seen to have very eccentric and inclined orbits.

In order to investigate the uniqueness of our Solar System, exoplanets need to be studied. Their evolution cannot be viewed directly as they form over millions of years. Planets form in the protoplanetary discs surrounding Young Stellar Objects (YSO's) and other pre-main sequence stars. Therefore, in order to investigate how planets form, the formation and evolution of protoplanetary discs are studied.

Micron sized dust grains in a protoplanetary disc can collide to accumulate and form millimetre sized grains. Past the snowline (the radius at which water forms ice) the dust grains gain an ice mantle envelope, increasing the possibility of the particles sticking upon collision. Once the particles reach millimetre sized they can begin to drift towards the star and may end up sublimating. As well as this, larger particles colliding with increasing velocities lead to fragmentation rather than

CHAPTER 1

cohesion, causing the particles to be broken up. These barriers can prevent the growth of dust to metre sized particles. The mechanism to overcome these barriers is still unknown. The evolution of planetesimals, km sized objects, to planets is hypothesised. The planetesimals and gas in the disc can gravitationally interact to form either terrestrial planets or the cores of gas giants.

This thesis focuses on trying to detect centimetre sized dust grains in the disc surrounding the YSO DG Tau B. Detecting centimetre sized particles in discs will help to determine under what circumstances discs overcome the *metre-sized barrier*. The radio interferometers e-MERLIN and EVLA are used to observe the protoplanetary disc.

1.1 Formation of Protoplanetary Discs

Regions of molecular gas and dust in the Interstellar Medium (ISM) form Giant Molecular Clouds (GMC). It is within these clouds that stars and planets form (Ward-Thompson & Whitworth 2011). GMC's can have radii of tens of parsecs and have masses of up to millions of solar masses. In order for stars to form, a molecular cloud needs to collapse. This depends on the relative strengths of the gravitational potential energy and the internal energy. Once the gravitational potential energy is greater than the internal energy the cloud may collapse. Smaller regions within the cloud will begin to fragment forming prestellar cores. These may go on to form individual stars. The collapse of a GMC can form many stars within a small radius, which we refer to as a stellar cluster.

Prestellar cores contract to form protostars. Objects that are not yet main sequence stars are referred to as Young Stellar Objects (YSO's). Lada (1987) proposed a classification system (Class I, II and III) for the different stages of protostellar evolution. Andre et al. (1993) later added a further Class 0 to the classification of Young Stellar Objects. The different classes of protostellar evolution are shown in Figure

CHAPTER 1

1.1. Protostars are difficult to observe in the optical as they are surrounded by dust and gas. Therefore, in order to study them, their long wavelength spectral energy distribution (SED) is looked at. An SED shows the relationship between flux distribution and frequency.

The class of a Young Stellar Object is determined by looking at the slope of the SED between the wavelength range of $2.2\mu m$ and $10 - 25\mu m$. This is defined as the spectral index, α and is given by Equation 1.1 (Lada 1987):

$$\alpha = \frac{d\log[\lambda F_\lambda]}{d\log[\lambda]} \quad (1.1)$$

Class 0 Young Stellar Objects are protostars that are still embedded in an infalling envelope of dust and gas. These protostars are only visible at infrared and millimetre wavelengths and are undetected at $\lambda < 10\mu m$ (Andre et al. 1993). They are also characterised by a low ratio of $L_{\text{Bolometric}}/L_{\text{Submm}}$ (Andre et al. 1993). This implies that the mass of the envelope surrounding the protostar is much greater than its mass.

Class I Young Stellar Objects have a spectral index $\alpha > 0$ (Lada 1987). The slowly rotating material in the envelope surrounding the pre-main sequence star begins to fall inwards due to gravity. As the size of the envelope decreases, conservation of angular momentum causes the cloud to rotate faster and flatten out to form a disc.

Class 0 and *Class I* protostars can remove angular momentum from the accreting protostar via outflows and jets. The YSO can accelerate a wind which can sweep up ambient gas, producing a CO outflow (Snell et al. 1980). Molecular outflows have been found to be bipolar or multipolar with a range of collimations (Lada 1985, Walker et al. 1988). A jet is formed when the disk wind travels at supersonic speeds (Pudritz & Norman 1983, 1986), which can interact with the surrounding material to produce knots of emission (Schwartz 1975). These objects are known as

CHAPTER 1

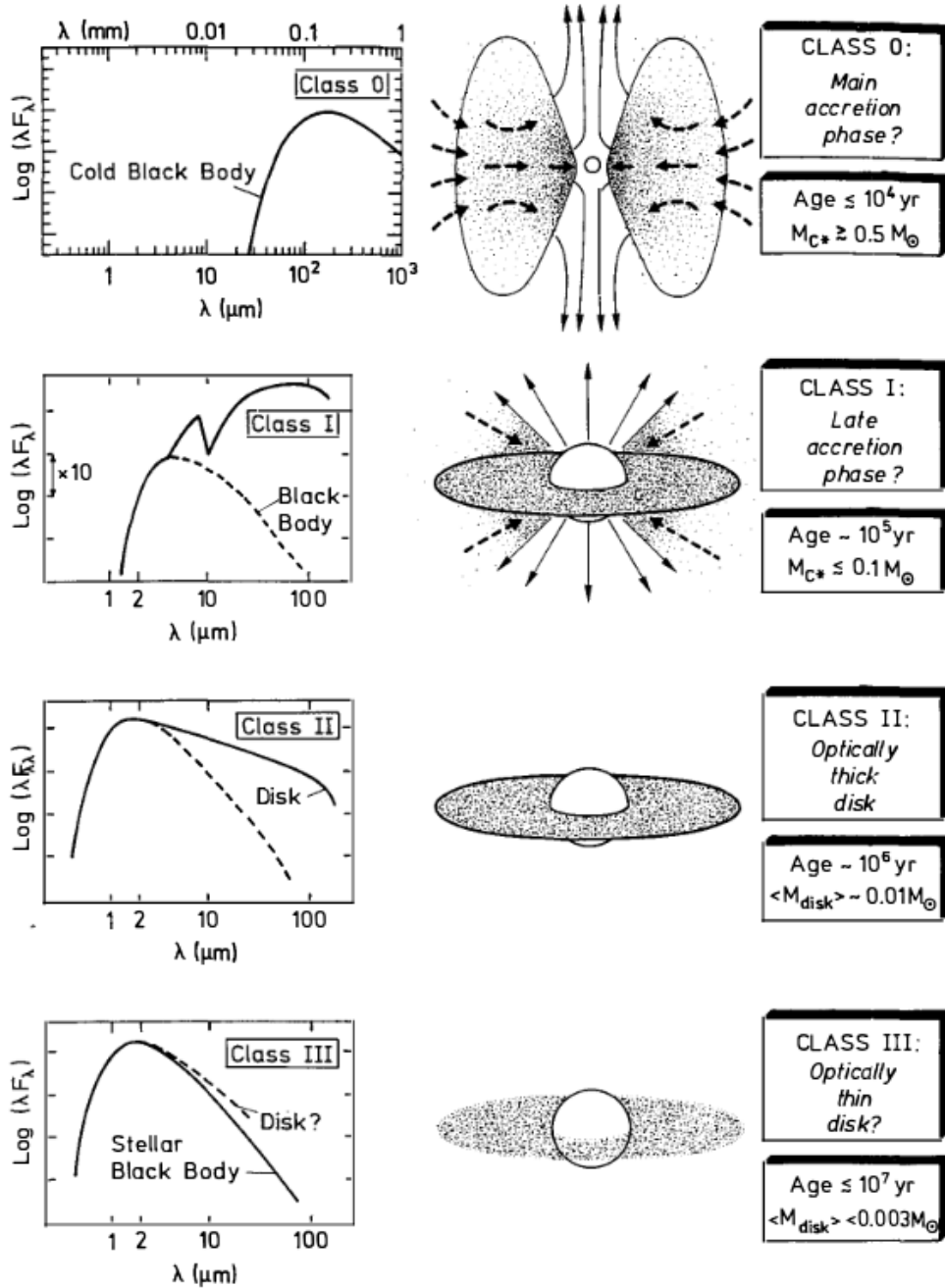


Figure 1.1: The evolutionary sequence of Young Stellar Objects, including their SED's (Andre 1994).

CHAPTER 1

Herbig-Haro objects (Herbig 1951, Haro 1952).

Class II Young Stellar Objects are also known as Classical T Tauri objects. These are pre-main sequence stars with a spectral index of $-1.5 < \alpha < 0$ (Lada 1987). These types of YSOs are formed when most of the material in the envelope has been dissipated and no longer accretes onto the disc (Andre et al. 1993). During this phase the protostar accretes at a reduced rate (Hartmann et al. 1998). Planet formation occurs mainly during this stage, and the removal of gas and dust begins in the protoplanetary disc.

The protoplanetary disc in this stage is cleared of dust and gas by many processes such as accretion onto the star, planet formation and photoevaporation of the disc (Hollenbach et al. 1994, Pollack et al. 1996). Photoevaporation occurs when ultraviolet radiation from the YSO heats up the surface of the disc. This causes the gas to unbind itself from the disc and leave as a wind (Hollenbach et al. 1994).

Class III Young Stellar Objects have a spectral index of $\alpha < -1.5$ and are known as Weak T Tauri stars (Lada 1987). They no longer have an envelope and are surrounded by a debris disc. This debris disc contains planetesimals (see Section 1.2), dust and molecular hydrogen (Bryden et al. 2009). The little amount of dust in the disc causes the infrared excess to be low, therefore the SED of Weak T Tauri stars shows emission predominantly due to the protostar.

1.2 Planetesimal Formation

The formation of planets from micron sized dust in a protoplanetary disc is a long process. The growth of μm -sized particles to mm and cm sized grains is well hypothesised, with lab based experiments agreeing with current core accretion theories (Blum & Wurm 2008, Beitz et al. 2011, Weidenschilling 1977). The formation of terrestrial and gas giant planets from kilometre sized planetesimals has been simulated

CHAPTER 1

and is understood to occur due to the mutual gravitational interactions of planetesimals. The precise mechanisms for forming planetesimals is still not well understood, mainly due to mm and cm dust collisions resulting in fragmentation rather than cohesion.

Micron sized dust grains are comprised of mostly silicates and are well coupled to the gas in the protoplanetary disc. They possess a relative velocity to the gas caused by Brownian motion. Collisions between nm and μm particles are able to occur since they travel with a small relative velocity with respect to each other. Blum & Wurm (2008) showed that μm -sized dust grains can stick upon collision, via various surface forces such as Van der Waals and electrostatic forces, provided the relative velocities between the particles is less than 1 m s^{-1} (Blum & Munch 1993). This leads to the formation of mm to cm sized particles.

There are many barriers that cm sized particles face whilst trying to grow to km sized planetesimals, including fragmentation and radial drift. As particles begin to grow in mass they decouple from the gas, causing them to travel with larger relative velocities with respect to the gas. Wurm et al. (2005) conducted an experiment in which mm particles were projected at cm dust targets. They found that for collisions below 13 m s^{-1} the mm particle rebounded and only a small degree of fragmentation occurred. They also observed that collisions occurring with a velocity of up to 25 m s^{-1} , resulted in approximately 50% of the mass of the projectile sticking to the target. The various outcomes of particle collisions are illustrated in Figure 1.2.

The “bouncing barrier” was first introduced by Blum & Munch (1993). They collided mm sized dust aggregates with velocities between 0.15 and 4 m s^{-1} , and found that the particles “bounced off” each other rather than combining. This can limit the growth of particles to cm sized particles (Windmark et al. 2012). The “bouncing barrier” can be overcome if there is a sufficient amount of cm particles in the disc to sweep up the smaller dust grains (Windmark et al. 2012).

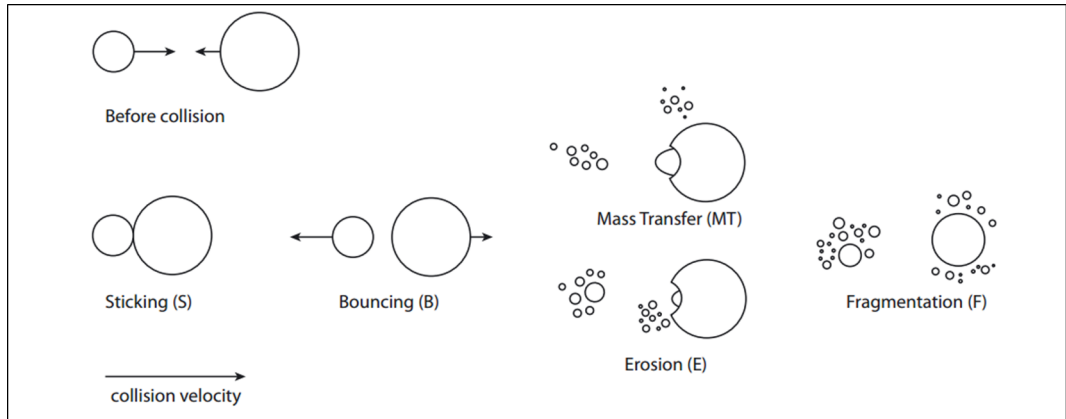


Figure 1.2: The different outcomes of particle collisions (Windmark et al. 2012).

The gas in the disc is supported by a gas pressure which prevents it from feeling the effects of the radial component of the stellar gravity. This causes the gas to travel at sub-Keplerian velocities (Testi et al. 2014). The dust in the disc is not supported by this pressure, therefore as the particles increase in mass and decouple from the gas their relative velocities with respect to the gas increases. This causes them to feel a head wind and begin to lose angular momentum (Weidenschilling 1977). The particles begin to drift towards the central YSO, and will either accrete onto the YSO or sublimate due to photoevaporation. Fragmentation, the “bouncing barrier” and radial drift halts particle growth to cm grains, a problem which has been coined the “meter barrier”.

1.3 Observations of Protoplanetary Discs

There are two types of continuum radiation; thermal and non-thermal. Thermal radiation relies solely on the temperature of the emitter and examples include black-body radiation and free-free emission. Non-thermal radiation, such as Compton scattering and synchrotron radiation, is independent of the temperature of the emitter.

CHAPTER 1

The dust in a protoplanetary disc emits thermal blackbody radiation. A blackbody is defined as an object that perfectly absorbs all wavelengths of light. A blackbody that is in thermal equilibrium will emit radiation with an intensity described by Planck's law, defined in Equation 1.2:

$$B_\nu(T) = \frac{2h\nu^3}{c^2} \frac{1}{e^{\frac{h\nu}{kT}} - 1}, \quad (1.2)$$

where k is the Boltzmann constant and h is the Planck constant. At long wavelengths, when $h\nu \gg kT$, a blackbody can be described by the Rayleigh-Jeans law. In this regime the dust is optically thin and the flux varies with frequency according to $F \propto \nu^2$. Wien's approximation describes the emission at shorter wavelengths when $h\nu \ll kT$ (Wien 1897). The dust is optically thick in the Wien regime.

Objects that do not absorb all the incident radiation perfectly and emits less energy than a blackbody are known as greybodies. They are characterised by their dust emissivity index β .

As the temperature of a blackbody decreases, so does its intensity. This causes the peak to move to lower frequencies. This is shown in Figure 1.3. The emission of a blackbody peaks at λ_{\max} and is related to temperature according to the equation:

$$\lambda_{\max} = \frac{b}{T}, \quad (1.3)$$

where b is Wien's displacement constant. This is known as Wien's displacement law. The total energy radiated by a blackbody per second per unit area, j^* is given by the Stefan-Boltzmann law,

$$j^* = \sigma T^4, \quad (1.4)$$

This defines the width of the peak of the blackbody curve.

The dust in a protoplanetary disc can be studied by looking at its infrared SED. It classifies objects by looking at the slope of the SED at wavelengths longer than

CHAPTER 1

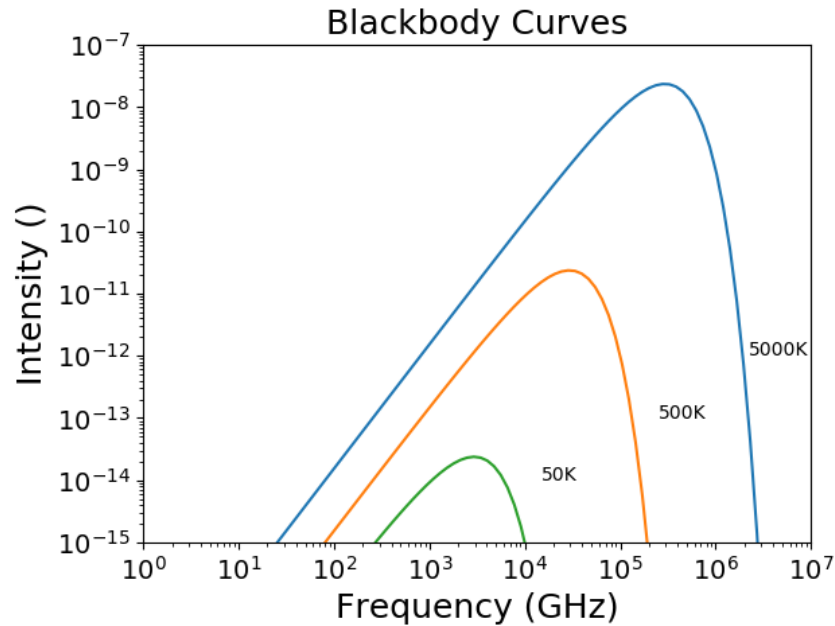


Figure 1.3: Planck's law for temperatures of 5000K, 500K and 50K. The emission at high frequencies is described by Wien's approximation whilst the Rayleigh Jeans law describes the emission at low frequencies.

$2\mu m$ (Lada 1987). YSO's emit UV radiation which may be absorbed by the dust in a protoplanetary disc. The dust then re-emits this light at longer wavelengths (Mendoza V. 1968). A detection of an infrared excess compared to the infrared emission from the star alone could be indicative of a protoplanetary disc.

Different physical regions in a protoplanetary disc are probed by different wavelength regimes, each of which affect different regions of the SED (see Figure 1.4). The hottest region of a protoplanetary disc is the inner region, closest to the YSO. The dust absorbs UV radiation and re-emits the light with wavelengths between 1 and $10\mu m$. This region of the disc can reach temperatures up to approximately 1500K.

The surface of a disc contains warm dust with approximate temperatures of 100-500 K. The dust absorbs radiation from the YSO and emits thermal radiation with

CHAPTER 1

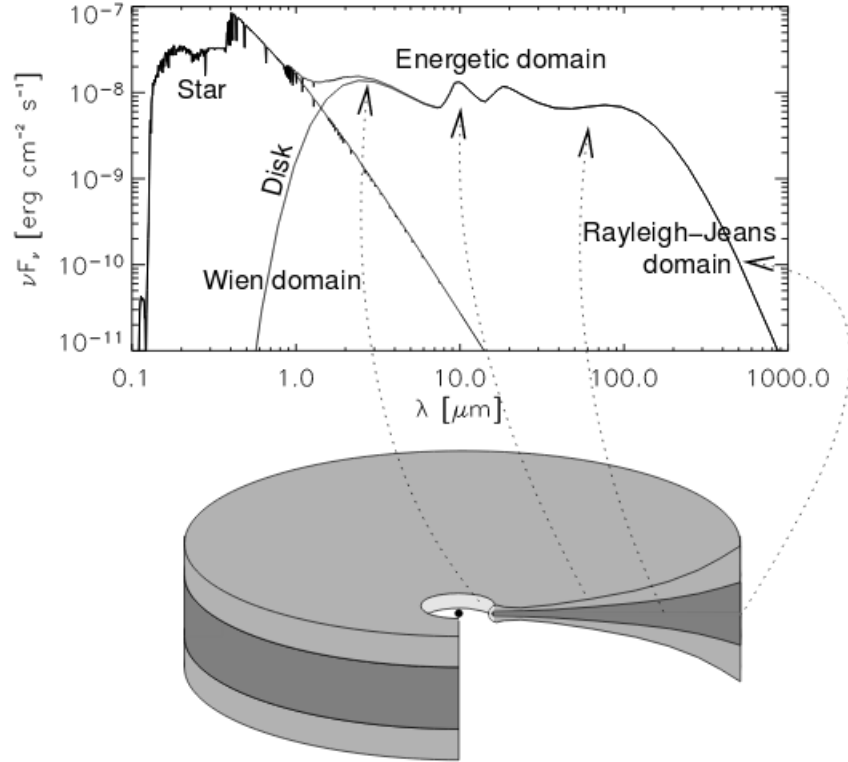


Figure 1.4: SED of a protoplanetary disc and the origin of various components. (Dullemond et al. 2007).

a wavelength range of $10 - 100\mu\text{m}$. The layers of dust below the surface will not be heated by the UV radiation, instead they absorb and re-emit the radiation emitted by the layers above (Adams et al. 1987, Kenyon & Hartmann 1987, Calvet et al. 1991, Malbet & Bertout 1991, Chiang & Goldreich 1997). Therefore the temperature of the dust grains decreases towards the midplane of a protoplanetary disc. The dust in the midplane has temperatures $< 50\text{K}$ and can be probed by sub-mm and mm observations.

The midplane of a protoplanetary disc contains most of the mass of the dust, and therefore is the best place to study the evolution of planet formation. The size distribution of the grains can be deduced by looking at the slope of the SED at millimetre wavelengths where $F_\nu \propto \nu^\alpha$, with $\alpha = 2 + \beta$. Draine (2006) showed that

CHAPTER 1

a spectral index of $2.0 < \alpha < 3.0$ at mm-cm wavelengths is indicative of particles approximately three times the observing wavelength. Whereas a spectral index of $-0.1 < \alpha < 1.0$ is indicative of stellar winds and jets. A high spectral index of $3.5 < \alpha < 4.0$ is due to grains of dust that have truncated at small sizes.

The flux density, F_ν , emitted by the dust can be estimated using Equation 1.5:

$$F_\nu = \frac{m_d \kappa_d(\nu) B_\nu(T)}{D^2}, \quad (1.5)$$

where D is the distance to the star, m_d is the mass of the dust, $B_\nu(T)$ is the blackbody intensity (Equation 1.2) and $\kappa_d(\nu)$ is known as the dust mass opacity coefficient (Hildebrand 1983). $\kappa_d(\nu)$ is given by:

$$\kappa_d(\nu) = \frac{3Q_\nu}{4a\rho_d}, \quad (1.6)$$

where Q_ν is the emission coefficient of the dust, a is the radius of a grain of dust and ρ_d is the density within a single dust grain.

Chapter 2

Radio Interferometry and e-MERLIN

2.1 Introduction to Radio Interferometry

The angular resolution of a telescope, ϑ , is given by the Rayleigh criterion (Rayleigh 1879):

$$\vartheta = 1.22 \frac{\lambda}{D}, \quad (2.1)$$

where λ is the operating wavelength of the telescope and D is the size of the aperture. In order to study small scale structures, such as protoplanetary discs, resolutions of approximately $\vartheta \leq 0.1$ arcsec are needed. At cm wavelengths, this requires km sized apertures, which is infeasible. In order to reach these small angular scales an interferometer can be used.

A radio interferometer is a collection of small radio telescopes that work together; combining the signal they each receive to simulate a large single radio telescope dish. The limiting factor for resolution in an interferometer is the maximum separation between the telescopes, b . This is known as the baseline length.

CHAPTER 2

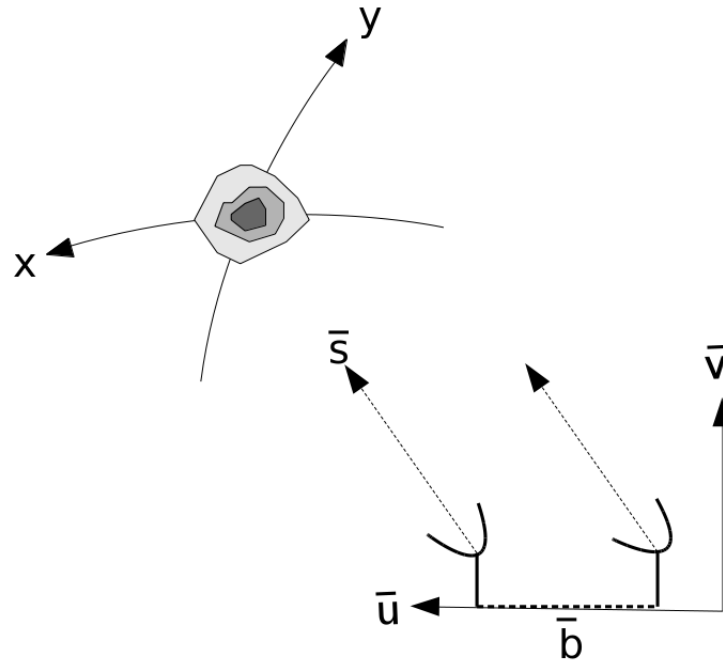


Figure 2.1: The relationship between the image plane and the (u,v) plane is shown here. \bar{s} is a unit vector in the direction of the object. \bar{b} is the baseline length between two telescopes of the array.

The antennae in the array cannot be placed closer than their physical sizes will allow. Therefore, there is a minimum baseline, b_{\min} , that causes a minimum resolution to be observed. This is known as the zero spacing problem. Structures larger than this resolution will not be resolved.

A different frame of reference is used in radio astronomy to view objects on the night sky (Figure 2.1). An antenna in an interferometer that is observing an object with right ascension, x and declination y , will point to the object in the direction given by \bar{s} . \bar{u} and \bar{v} represent the east-west and north-south components of the interferometer's projected baseline onto the plane of the sky.

An object being observed by a radio interferometer in the direction \bar{s} will have an intensity $I(\bar{s})$ on the night sky. An interferometer measures the Fourier transform of this intensity pattern. For any given observation, a wavefront from the source

CHAPTER 2

will not usually arrive at each antenna simultaneously.

To ensure that the signals received by each antenna due to the same wavefront are added correctly, a geometric delay is added to each antenna's signal. The geometric delay between antennae receiving the wavefront from the source is given by

$$\tau_g = \frac{\bar{b} \cdot \bar{s}}{c}, \quad (2.2)$$

where c is the speed of light and \bar{s} is a unit vector in the direction of the object (Burke & Graham-Smith 1997). The correlator does not receive the signals from each antenna at the same time, therefore there is an instrumental delay, τ_i , that is also applied to each antenna.

For a two element array, the signals received by each antenna are outputted as voltages where:

$$V_1 \propto v_1 \cos[2\pi\nu(t - \tau_g)] + i \sin[2\pi\nu(t - \tau_g)], \quad (2.3)$$

$$V_2 \propto v_2 \cos[2\pi\nu t] + i \sin[2\pi\nu t], \quad (2.4)$$

where v_1 and v_2 are the voltage amplitudes, τ_g is the geometric delay, and ν is the frequency of the observations (Rohlfs & Wilson 2000).

The voltage outputs are then passed through a correlator where they are cross-multiplied and time averaged giving:

$$R_c \propto \frac{v_1 v_2}{2} \cos[2\pi\nu\tau_g] + i \sin[2\pi\nu\tau_g], \quad (2.5)$$

For a source of intensity $I(\bar{s})$ observed using antennae of collecting area $A(\bar{s})$, the output of the correlator is given by

$$R = A(\bar{s}) I(\bar{s}) \{ \cos[2\pi\nu\tau] + i \sin[2\pi\nu\tau] \} d\bar{s} d\nu, \quad (2.6)$$

CHAPTER 2

where τ is the difference between the geometric and instrumental delays (Rohlf & Wilson 2000). Integrating over \bar{s} , the total response of the correlator is given by:

$$R = \iint_{\bar{s}} A(\bar{s})I(\bar{s})\{\cos[2\pi\nu\tau] + i\sin[2\pi\nu\tau]\}d\bar{s}d\nu, \quad (2.7)$$

When making an observation with an interferometer, the field of view is centred on the position \bar{s}_0 . This is called the phase tracking centre (Thompson 1989) and is given by:

$$\bar{s} = \bar{s}_0 + \bar{\sigma}, \quad (2.8)$$

Substituting Equation 2.8 into Equation 2.7 and replacing τ_g with Equation 2.2 yields:

$$R = \exp\left[i2\pi\nu\left(\frac{\bar{b} \cdot \bar{s}_0}{c} - \tau_i\right)\right]d\nu \iint_{\bar{s}} A(\bar{\sigma})I(\bar{\sigma})\exp\left[i2\pi\nu\left(\frac{\bar{b} \cdot \bar{\sigma}}{c}\right)\right]d\sigma, \quad (2.9)$$

where the integral in Equation 2.9 is known as the visibility function, V (Rohlf & Wilson 2000).

The van Cittert-Zernike theorem (van Cittert 1934, Zernike 1938) relates the visibility function measured in (u, v) space to the intensity distribution.

$$V(u, v) = \iint I(x, y)e^{-2\pi i(ux+vy)}dxdy, \quad (2.10)$$

where $I(x, y)$ is the intensity distribution. Therefore, the visibility that an interferometer measures is the Fourier transform of the intensity distribution on the sky.

Not all regions of the focal plane will be used when making observations using an interferometer. Baselines between antennae are fixed due to an interferometer being made of individual antennae. This causes the (u, v) plane to only be partially sampled. In order to produce an image with as few artefacts as possible, a well

CHAPTER 2

sampled (u, v) plane is needed. If there are N antennae in an array, the number of available baselines is given by:

$$N_b = \frac{1}{2}N(N - 1), \quad (2.11)$$

In order to increase the (u, v) plane coverage and number of baselines, either more antennas are needed or the antennas can be moved periodically as the observations are made. As well as this, as the Earth rotates more regions of the focal plane are used. Therefore, longer observing times will ensure that the (u, v) plane is better sampled. The process of trying to fill the (u, v) plane is known as aperture synthesis.

The visibility is sampled at discrete points on the (u, v) plane. The sampling function, $S(u, v)$, is described by a delta function that gives unity to all the sampled positions in the (u, v) plane and zero to everything else. The initial image that is produced after an observation is known as the dirty image and is given by:

$$I^D(x, y) = \int \int V(u, v) \cdot S(u, v) e^{2\pi i(ux+vy)} dudv, \quad (2.12)$$

where $V(u, v)$ is the complex visibility and $S(u, v)$ is the sampling function (Clark 1989). The convolution theorem states that the product of two Fourier transforms is equal to the Fourier transform of their convolution. Therefore, the dirty image can also be expressed as:

$$I^D(x, y) = S(x, y) \otimes I(x, y), \quad (2.13)$$

where $S(x, y)$ is the Fourier transform of the sampling function and is given by:

$$S(x, y) = \int \int S(u, v) e^{2\pi i(ux+vy)} dudv, \quad (2.14)$$

This is known as the point spread function or dirty beam (Clark 1989). In order to obtain the intensity distribution, $I(x, y)$, the dirty beam needs to be deconvolved from the dirty image.

2.2 Calibrating Radio Interferometric Data

Each telescope in an interferometer responds differently to the incoming signals from the astronomical source. This is due to the variation in each telescope's size as well as their individual efficiencies. As well as this, the atmosphere will affect the signals reaching the antennae. In order to improve the fidelity of the final image, the data needs to be calibrated. Calibrating radio interferometric data involves:

- Initial calibration
- Delay calibration
- Bandpass calibration
- Flux calibration
- Gain calibration

Initial calibration involves removing the first few seconds of data from each telescope. This is done to remove systematic errors that occur during the initial stage of the observation. This process is known as “quacking”. The data are also inspected to find any obvious bad data. This could be caused by errors in an individual antenna or a particular baseline. If an individual antenna was responsible for the majority of the bad data it should be deleted. However this will reduce the sensitivity of the observation.

Inaccuracies in the position of the telescopes will cause the phase to vary as a function of frequency. This will affect the accuracy of the sky representation. *Delay calibration* can be applied to accurately determine the phase as a function of frequency.

Each antenna has a unique phase and amplitude response to the incoming signal. *Bandpass calibration* can be conducted to correct any errors that the amplitude and

CHAPTER 2

phase have as a function of frequency. The bandpass and delay calibrations can both be done using a point source with a high brightness. It will need to be observed for a short period of time in order to determine the relationship between phase and frequency.

Flux Calibration is required to scale the amplitudes correctly and convert the the signal to conventional units such as Janskys ($1\text{Jy} = 10^{-26}\text{Wm}^{-2}\text{Hz}^{-1}$). A bright source with a known flux density is observed when making flux calibrations.

Gain calibration is performed to correct the time dependent phase and amplitude data which have been affected by the atmosphere or the instruments. A source that is close to the target source, has a known structure and a moderately strong intensity can be used for this calibration. Examples include quasars and planets. Observations need to be conducted frequently to find the atmospheric phase change to the line of sight of the target.

All sources used for the calibrations need to be close to the target object. This is because the antenna response may be affected by several factors such as opacity of the atmosphere and aperture illumination.

From Equation 2.14 we saw that in order to obtain the true sky brightness, the dirty beam needs to be deconvolved from the dirty image. This deconvolution can be done using the CLEAN algorithm proposed in 1974 (Högbom 1974). This algorithm assumes the sky is made up of a series of point sources. It iteratively finds the position and strength of these sources and removes them until a set threshold is reached. The final image produced will be a sum of the “CLEANED” sources and a “CLEANED” beam.

CHAPTER 2

Table 2.1: e-MERLIN capabilities in the C band (Garrington et al. 2004)

	C Band (4-8 GHz)
Resolution (mas)	40
Field of View (arcmin)	7
Bandwidth (GHz)	2
Sensitivity in a full imaging run ($\mu\text{Jy/Bm}$)	1.8-2.3

2.3 e-MERLIN

The observations used in this thesis were taken with the extended Multi-Element Radio Linked Interferometer Network (e-MERLIN). This is an array of seven telescopes situated across England (Figure 2.2), with the central correlator situated at the Jodrell Bank Observatory. The array includes the Lovell and Mark II telescopes at the Jodrell Bank Observatory, and radio telescopes in Defford, Knockin, Pickmere, Darnhall and Cambridge.

The interferometer is capable of conducting astrometric, polarimetric and spectroscopic observations. It has a resolution of 10 – 150 milliarcsec (mas) and a sensitivity of approximately $1 \mu\text{Jy}$. e-MERLIN operates at three observing bands; 1.3 - 1.8 GHz, 4-8 GHz and 22-24 GHz (L,C and K bands respectively). Continuum observations for this thesis were conducted in the C band and the capabilities of e-MERLIN at this band can be found in Table 2.1.

The observations in this thesis were conducted as part of the Planet Earth Building-Blocks - a Legacy e-MERLIN Survey (PEBBLeS). It plans to image the discs around nineteen young stellar objects with the aim of detecting cm emission. This thesis will focus on the YSO DG Tau B.

CHAPTER 2

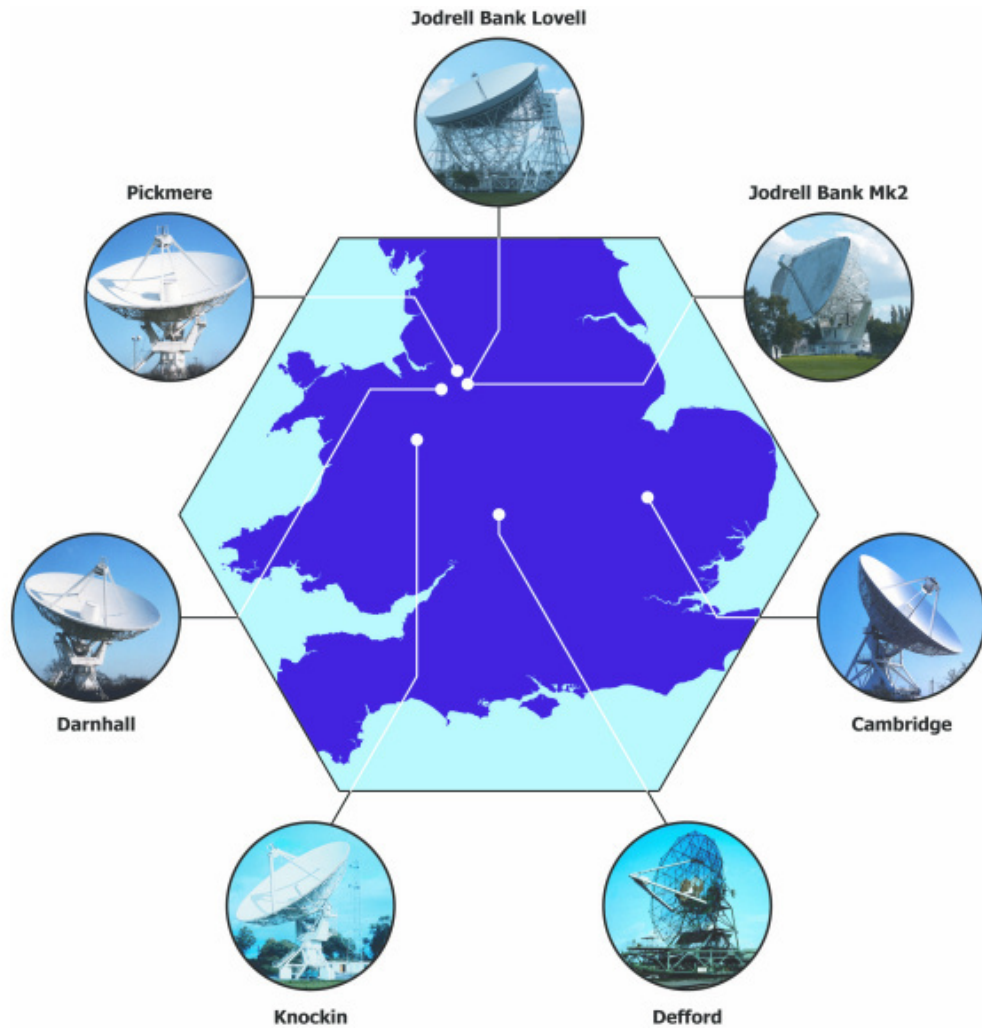


Figure 2.2: The interferometer e-MERLIN consists of seven telescopes situated across England.

2.4 EVLA

Observations for this thesis have also been taken with the Expanded Very Large Array (EVLA). The EVLA is an interferometer situated at the National Radio Astronomy Observatory in New Mexico, America. It is comprised of twenty seven radio antennae, each with a diameter of 25m. The antennae are positioned in a Y-shaped configuration (see Figure 2.3). The location of each antenna can be altered in order to increase or decrease the maximum baseline; this will depend on the resolution needed for the observations. There are four possible configurations of the EVLA; A,B,C and D. The A configuration of the EVLA has the longest maximum baseline at 36.4Km, whilst the D configuration has the shortest at 1.03Km. Therefore, the EVLA in the D configuration is able to resolve structures of a larger angular scale than the A configuration.

The interferometer is capable of astrometric, polarimetric and spectroscopic observations and has a sensitivity of $\approx 1\mu$ Jy in a 9hr observation. The EVLA can operate at eight different frequency bands, ranging from the L band at 1.0-2.0GHz to the Q band at 40.0-50.0GHz. Observations for this thesis were conducted using the Ka band in the D configuration. The capabilities of the EVLA during the observation can be found in Table 2.2.

The observations conducted in this thesis were part of the Disks@EVLA project (<https://safe.nrao.edu/evla/disks/>). This project aims to investigate millimetre and centimetre emission from large dust grains in the discs surrounding sixty six pre-main sequence stars.

CHAPTER 2



Figure 2.3: The EVLA interferometric array consists of twenty seven telescopes in a Y-shaped configuration. Each telescope is 25 m in diameter. Image from NRAO/AUI.

Table 2.2: EVLA capabilities in the Ka band (Perley et al. 2011)

	Ka Band
Frequency Range (GHz)	26.5-40.0
Bandwidth (GHz)	8
Sensitivity ($1\sigma/hr$) ($\mu\text{Jy/Bm}$)	3.2
D Configuration	
Maximum Baseline Separation (km)	1.03
Minimum Baseline Separation (km)	0.035

Chapter 3

A cm Study of DG Tau B

3.1 Previous Studies of DG Tau B

This thesis will focus on the disc surrounding the young stellar object DG Tau B, located 150pc away in the constellation of Taurus. The spectral energy distribution of DG Tau B has previously been studied and it was found to be a Class I young stellar object (Watson et al. 2004, Luhman et al. 2010). The SED of DG Tau B has been modelled using a $0.5M_{\odot}$, $2.5R_{\odot}$ star at 4000K (Gramajo et al. 2010). It is located approximately $1'$ SW from the classical T Tauri star DG Tau A (Jones & Cohen 1986, Eislöffel & Mundt 1998, Torres et al. 2009, Luhman et al. 2010, Rodríguez, Dzib, Loinard, Zapata, Raga, Cantó & Riera 2012). It is suspected that the two pre main sequence stars are unrelated except by projected proximity (Jones & Cohen 1986).

Mundt & Fried (1983) first detected the Herbig Haro jet powered by DG Tau B and named it HH159. This is an asymmetric bipolar jet that has been imaged at optical and infrared wavelengths (Eislöffel & Mundt 1998, Stapelfeldt et al. 1997). The red optical lobe of the jet has a chain of bright knots that extend $55''$ to the NW of DG Tau B. The blue lobe is less collimated and fainter and only extends $10''$ to the SE (Mundt et al. 1991, Eislöffel & Mundt 1998).

CHAPTER 3

DG Tau B also features a $^{12}\text{CO}(3-2)$ molecular outflow first detected by Mitchell et al. (1994). They report the outflow being spatially aligned to the jet as well as the momentum transport rates of the jet and outflow being similar. They conclude that the molecular outflow is formed by ambient gas being swept up by the fast collimated jet. The redshifted CO emission extends approximately $40''$ NW from DG Tau B, whilst the blueshifted emission only extends approximately $3''$ (Mitchell et al. 1997).

Perpendicular to the jet and molecular outflow of DG Tau B is a circumstellar disc (Stapelfeldt et al. 1997, Padgett et al. 1999). The disc is close to edge on at $64 \pm 2^\circ$ (Guilloteau et al. 2011) and at optical wavelengths it is optically thick (Stapelfeldt et al. 1997).

Zapata et al. (2015) conducted $^{12}\text{CO}(2-1)$ line and 1.3mm continuum observations of DG Tau B with the Submillimetre Array (SMA) (see Figure 3.1). The redshifted NW molecular outflow detected by Mitchell et al. (1994) can be seen as well as its distinctive ‘V’ shaped morphology. Hubble Space Telescope (HST) measurements by Stapelfeldt et al. (1997) at ≈ 800 nm and ≈ 670 nm have been overlaid on this image and show the SE component of the jet from DG Tau B. The SMA 1.3mm continuum observations have detected the circumstellar disc surrounding DG Tau B, previously detected lying perpendicular to the jet and outflow (Stapelfeldt et al. 1997, Padgett et al. 1999). The contours range in steps of 15% from 25% to 85% of the peak emission.

3.2 New data : Observations with e-MERLIN

Observations of DG Tau B were taken with e-MERLIN in 2014 and 2016; at 6.48GHz (4.63cm) and 7.25GHz (4.14cm) respectively. The data were calibrated following the processes outlined in Section 2.2. The data were then deconvolved using *CLEAN* in the *Common Astronomy Software Applications* (CASA) package.

CHAPTER 3

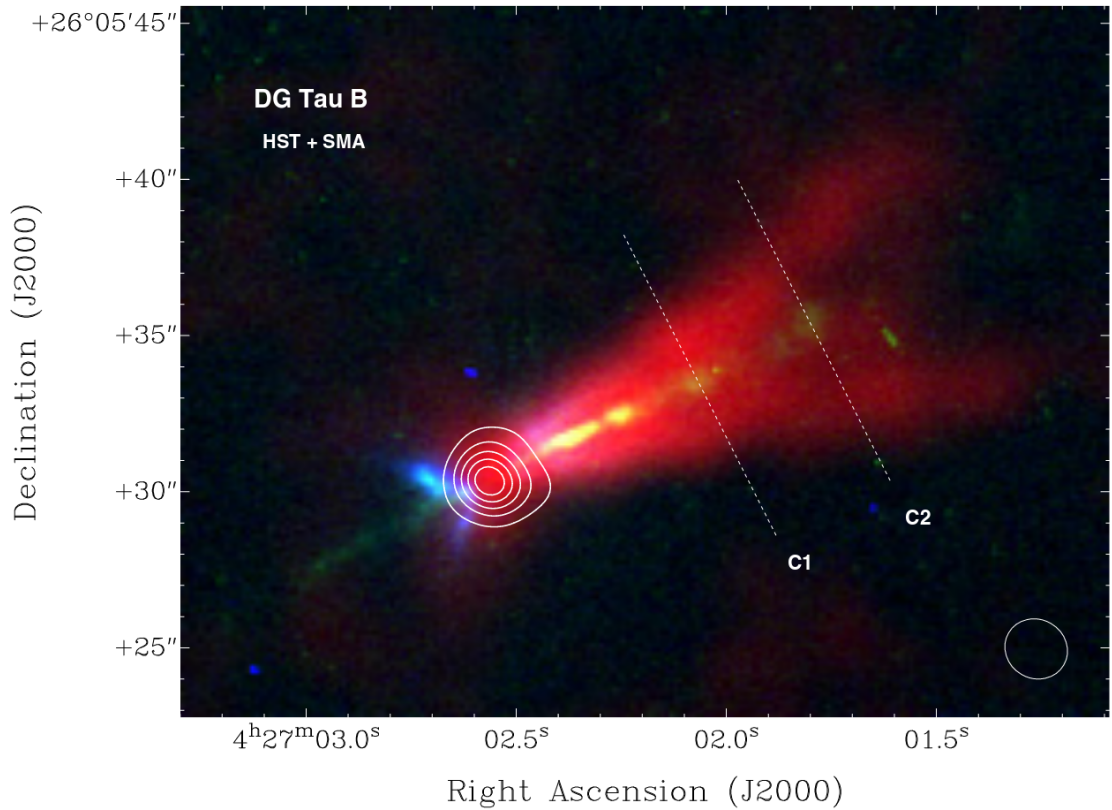


Figure 3.1: SMA observations at 1.3mm by Zapata et al. (2015) show the disc of DG Tau B (contour). The peak continuum emission is $0.31 \text{ Jy beam}^{-1}$ and the contours range in steps of 15% from 25% to 85% of the peak emission. SMA ^{12}CO emission of the molecular outflow (red) traces the DG Tau B jet. C1 and C2 indicate where position-velocity measurements were made by Zapata et al. (2015). Observations taken using the HST Wide-Field Planetary Camera 2 conducted by Stapelfeldt et al. (1997) are also shown. Observations were taken at $\approx 800\text{nm}$ (blue) and $\approx 670\text{nm}$ (green).

CHAPTER 3

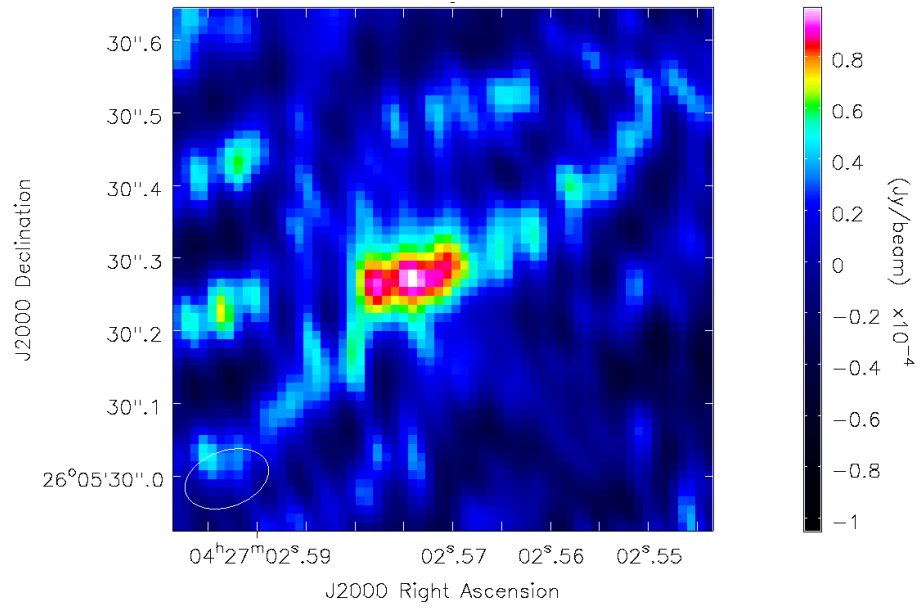
Data taken with the Jodrell Bank Lovell Telescope were not included in the final observations. During the “quacking” stages of calibration, (see Section 2.2), a significant amount of the data from the start of the observation contained systematic errors. There were also many outliers in the amplitude and phase plots produced during the bandpass calibration staged. Therefore, the observations taken with the Lovell Telescope were removed; this reduced the sensitivity of the observations.

The final cleaned images are shown in Figures 3.2a and 3.2b. The beam for each observation is shown in the lower left corner. Residuals from the cleaning process can be seen in both observations, although they are more prominent in the 2016 epoch than the 2014. The 2014 data still contain some artefacts. However, attempts to remove them significantly affected the quality of the observation of DG Tau B. An elongated structure can be seen in both observations, with the NW component being more prominent in the 2014 epoch than the 2016. Comparing Figures 3.2a and 3.2b to the observation made by Zapata et al. (2015), the orientation of the structure appears to be in the same direction as the DG Tau B jet and molecular outflow.

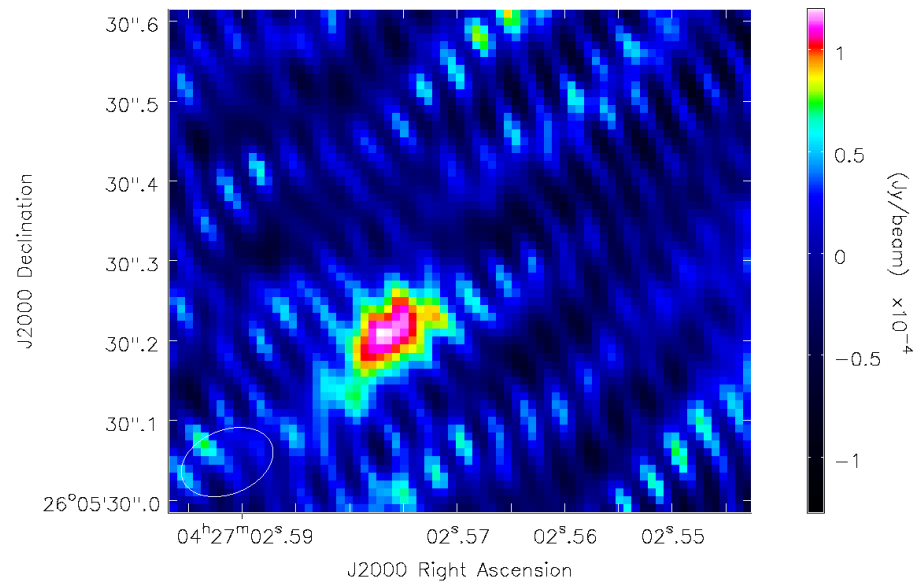
Two-dimensional elliptical Gaussian components were fit to DG Tau B in each epoch to determine parameters of the system. This was done in *CASA* using *imfit*. We found that DG Tau B had a position of $\alpha_{J2000.0} = +04^h27^m02.574^s \pm 0.001^s$, $\delta_{J2000.0} = +26^\circ05'30.274'' \pm 0.004''$ in 2014 and $\alpha_{J2000.0} = +04^h27^m02.576^s \pm 0.001^s$, $\delta_{J2000.0} = +26^\circ05'30.211'' \pm 0.005''$ in 2016. DG Tau B appears to have moved between the two epochs which could be due the proper motion of the system.

We found that the flux density and peak intensity values of DG Tau B are $204 \pm 26 \mu\text{Jy}$ and $98.4 \pm 8.8 \mu\text{Jy beam}^{-1}$ respectively in 2014 and $158 \pm 23 \mu\text{Jy}$ and $121 \pm 11 \mu\text{Jy beam}^{-1}$ in 2016. We also find from this fit that the source has a deconvolved size of $133 \times 74 \pm 27 \times 18$ mas with a position angle of $106 \pm 18^\circ$ in 2014. In 2016, the source has a deconvolved size of $153 \times 83 \pm 32 \times 11$ mas with a position angle of $130 \pm 8^\circ$. Table 3.1 outlines the parameters found from the Gaussian fit.

CHAPTER 3



(a) DG Tau B taken with e-MERLIN in 2014 at 6.48GHz. The beam, shown in the lower left, is $0.12 \times 0.08''$ with a position angle of -69.9°



(b) DG Tau B taken with e-MERLIN in 2016 at 7.25GHz. The beam, shown in the lower left, is $0.12 \times 0.08''$ with a position angle of -68.0°

Figure 3.2: e-MERLIN Observations of DG Tau B taken in 2014 (top) and 2016 (bottom).

CHAPTER 3

Table 3.1: Parameters of DG Tau B found by fitting elliptical Gaussians to the data.

Parameter	2014	2016
RA (J2000) $04^h27^m(s)$	02.574 ± 0.001	02.576 ± 0.001
Dec (J2000) $+26^\circ05'(\prime\prime)$	30.274 ± 0.004	30.211 ± 0.005
Deconvolved Major Size (mas)	133 ± 27	153 ± 32
Deconvolved Minor Size (mas)	74 ± 18	83 ± 11
Position Angle ($^\circ$)	106 ± 18	130 ± 8
Integrated Flux (μJy)	204 ± 26	158 ± 23
Peak Flux ($\mu\text{Jy beam}^{-1}$)	98.4 ± 8.8	121 ± 11
Frequency (GHz)	6.48	7.25

3.3 Spectral Energy Distribution

Previous observations of DG Tau B have been conducted at near-infrared, submillimetre and centimetre wavelengths (see references in Table 3.2). The flux densities of DG Tau B detected in these previous studies as well as in this work are outlined in Table 3.2.

An SED of DG Tau B was plotted (see Figure 3.3) using the data in Table 3.2. The dust in the disc may not perfectly absorb all incident radiation and therefore acts like a modified blackbody (or a greybody). Equation 1.5 outlined in Section 1.3 describes the flux density emitted by a modified blackbody. This equation as well as the Python curve-fitting routine *LMFIT* were used to fit a greybody curve on the SED.

Following Rodríguez, Dzib, Loinard, Zapata, Raga, Cantó & Riera (2012) we adopted a distance of 150 pc to DG Tau B. This distance is based on parallax measurements to both the L1495 region (131.5 pc; Torres et al. 2007, 2012) and HP

CHAPTER 3

Table 3.2: Flux values from previous observations of DG Tau B used in the SED.

Frequency (GHz)	Wavelength (mm)	Flux (mJy)	Detector	References
245731.50	0.001	1.95 ± 0.19	2MASS	(1)
183921.80	0.002	5.91 ± 0.59	2MASS	(1)
136891.50	0.002	14.24 ± 1.42	2MASS	(1)
83275.70	0.004	90.62 ± 5.00	IRAC	(2)
66620.50	0.005	287.88 ± 15.88	IRAC	(2)
51688.40	0.006	571.47 ± 21.04	IRAC	(2)
37474.10	0.008	830.28 ± 22.93	IRAC	(2)
12491.40	0.024	4641.7 ± 99.2	MIPS	(1)
4284.75	0.070	7836.0 ± 783.6	MIPS	(1)
230.61	1.300	531.4 ± 0	IRAM	(3)
111.03	2.700	83.6 ± 12.4	IRAM	(3)
42.83	7.000	3.57 ± 0.29	VLA	(4)
34.00	8.817	1.63 ± 0.087	EVLA	(5)
23.06	13.000	1.23 ± 0.03	VLA	(4)
17.63	17.004	0.735 ± 0.078	AMI-LA	(6)
16.87	17.771	0.645 ± 0.060	AMI-LA	(6)
16.12	18.598	0.595 ± 0.052	AMI-LA	(6)
15.37	19.505	0.555 ± 0.045	AMI-LA	(6)
14.99	20.000	0.80 ± 0.13	VLA	(4)
14.62	20.505	0.523 ± 0.049	AMI-LA	(6)
8.57	35.000	0.36 ± 0.02	VLA	(7)
8.33	36.000	0.46 ± 0.05	VLA	(4)
7.25	41.344	0.158 ± 0.023	e-MERLIN	(5)
6.48	46.276	0.204 ± 0.026	e-MERLIN	(5)
4.67	61.95	0.150 ± 0.063	e-MERLIN	(8)

References. (1) Robitaille et al. (2007), (2) Hartmann et al. (2005), (3) Guilloteau et al. (2011), (4) Rodmann et al. (2006), (5) This work, (6) AMI Consortium et al. (2012), (7) Rodríguez, Dzib, Loinard, Zapata, Raga, Cantó & Riera (2012), (8) Ainsworth et al. (2013)

CHAPTER 3

Tau (161 pc; Torres et al. 2009). Following Beckwith et al. (1990) and assuming a gas-to-dust ratio of 100 : 1, the mass opacity coefficient, $\kappa_d(\nu)$, was determined using:

$$\kappa_d(\nu) = 0.1 \left\{ \frac{\nu}{\nu_{central}} \right\}^{\beta_{disc}} \text{ cm}^2 \text{ g}^{-1}, \quad (3.1)$$

where $\nu_{central} = 10^{12}$ Hz. Previous observations of protoplanetary discs have determined their opacity spectral indices $\beta_{disc} \approx 1$ (Beckwith & Sargent 1991, Andrews & Williams 2005), therefore β_{disc} in the equation above was fixed at this value. There is still some debate in regards to the true value of β for protoplanetary discs; this will be discussed in Chapter 5.

A modified blackbody was fit to the emission from DG Tau B using a temperature of $T=9.6 \pm 0.6$ K and a mass of $M=0.30 \pm 0.03M_{\odot}$. The emission from DG Tau B at wavelengths smaller than submillimetre can be attributed to hotter dust closer to the central YSO (Dullemond et al. 2007), as well as the emission from DG Tau B. This project is only interested in the cold dust in the protoplanetary disc. The dust emits radiation at mm and cm wavelengths, therefore the SED was only modelled at long wavelengths.

An excess of emission can be seen at radio frequencies in the SED. This excess radiation could be due to thermal emission emitted by cm sized dust grains in the disc surrounding DG Tau B or non-thermal emission emitted by the DG Tau B jet. The excess emission could also be attributed to photoevaporative winds; formed when gas in the protoplanetary disc is heated and accelerated to thermal escape velocities. The radio excess was fit using a power law and the slope of the SED, i.e. the spectral index α , at cm wavelengths was calculated in order to determine the grain size distribution. The gradient of the radio excess was calculated to be $\alpha = 1.4 \pm 0.2$. The radio excess is a combination of free-free/synchrotron emission ($\alpha_{free-free/sync} = 0.3 \pm 0.2$) and thermal greybody radio ($\alpha_{greybody} = 3.0 \pm 0.1$).

CHAPTER 3

Following Draine (2006) where a spectral index of $2.0 < \alpha < 3.0$ is indicative of large dust grains and a spectral index of $-0.1 < \alpha < 1.0$ can be attributed to stellar winds and jets, we suspect that we have detected the DG Tau B jet rather than the disc. Analysis of the e-MERLIN observations were then conducted in order to confirm this.

3.4 Cross Cut Analysis

The e-MERLIN observations were studied in order to determine if the DG Tau B disc and/or jet had resolved. The full width half maximum of the DG Tau B at both epochs were found. This was done by fitting 2D Gaussian models to the observations, using the IDL routine *MPFIT2DPEAK*. The results from the Gaussian models can be found in Table 3.3.

The major axis is aligned parallel to the elongated structure of DG Tau B. Comparing our observations to those made by Zapata et al. (2015), we assume that the major axis lies in the direction of the jet of DG Tau B. The angle of the major axis from the x-axis has changed between the two epochs. This may imply that the jet of DG Tau B is either precessing or it may be an effect of the proper motion of the source. The proper motion of DG Tau B will be studied in Chapter 5.

In order to improve the signal to noise of the morphological structure of the DG Tau B disc, the two epochs of e-MERLIN data were combined. The position of DG Tau B has changed between the two observations (see Table 3.1), therefore the two epochs were first aligned in *CASA*. The separation between the co-ordinates of the peak emission in each epoch were found. This was added onto the reference co-ordinate of the 2016 data to align the 2016 data with the 2014. The 2016 epoch was aligned to the 2014 as the latter had better signal to noise.

The 2016 observation was then rotated in order to align the jet of DG Tau B in both epochs. The extent to which the jet has rotated was found by finding the

CHAPTER 3

Table 3.3: Parameters of DG Tau B found by fitting 2D Gaussian models to the two epochs of data. The angle of the major axis is measured anticlockwise from north.

Epoch	FWHM of Major Axis (mas)	FWHM of Minor Axis (mas)	Angle of Major Axis ($^{\circ}$)
2014	156.7 ± 4.2	96.9 ± 2.6	112.7 ± 4.6
2016	140.0 ± 5.0	103.2 ± 2.5	131.6 ± 3.4
Combined	164.7 ± 7.3	90.5 ± 3.6	114.0 ± 5.2

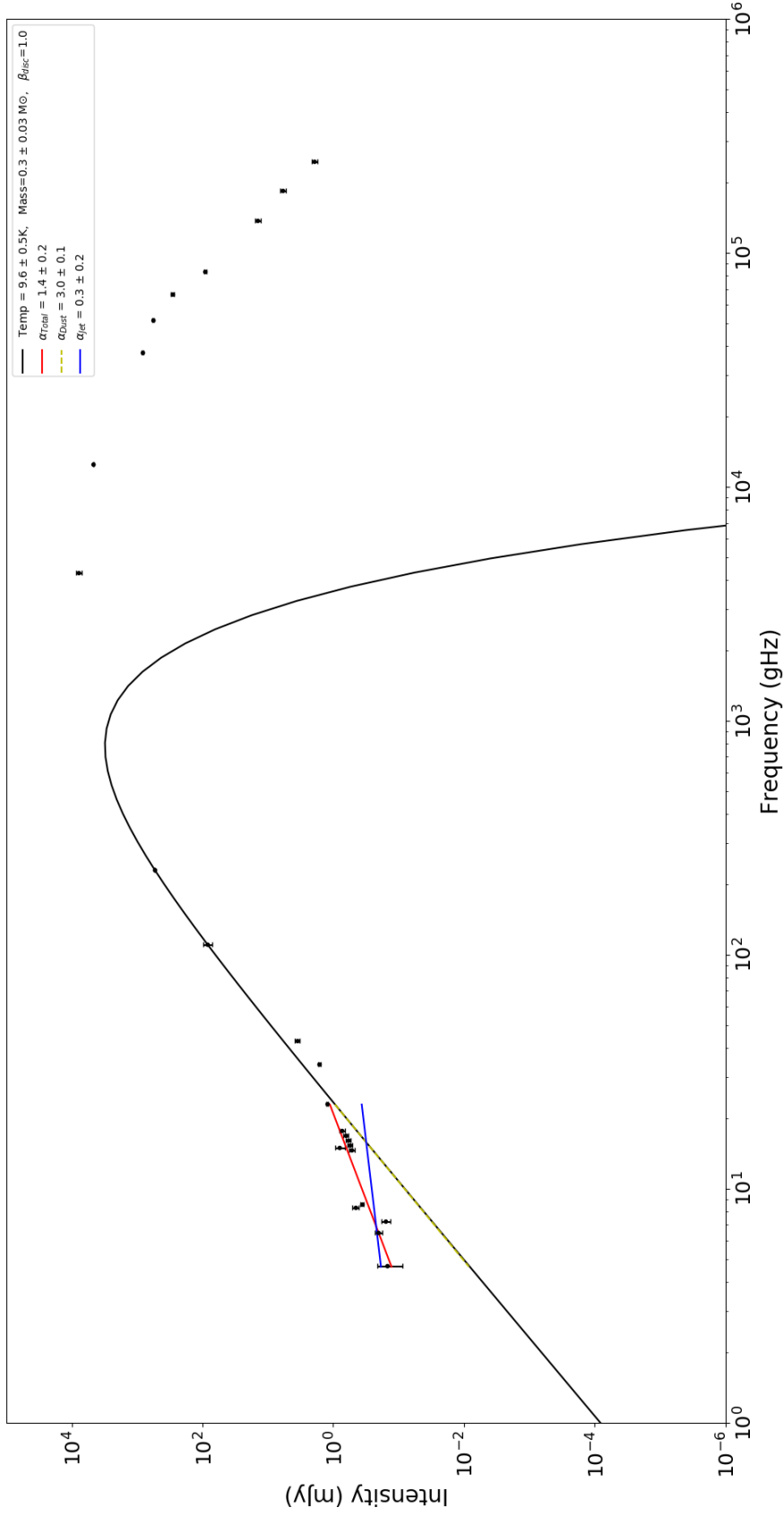


Figure 3.3: SED of DG Tau B plotted using observations made in this thesis and archive data. A modified blackbody has been fitted to the dust emission from DG Tau B. The dust has been modelled with a temperature of $T=9.6 \pm 0.6K$ and a mass of $m=0.3 \pm 0.03M_{\odot}$. The radio excess (red) is a combination of free-free emission (blue) and thermal greybody emission (yellow).

CHAPTER 3

difference between the angle of the major axis in both epochs. The 2016 observation was rotated by 18.9° to ensure the jet was aligned in both epochs. The two observations were then added and averaged to produce Figure 3.4.

The elongated structure is still visible in the combined image and there appears to be no improvement to the structure perpendicular to this. In order to determine if combining the observations resolved the disc and/or jet of DG Tau B or not, the FWHM of the emission both parallel and perpendicular to the disc was determined. This was done by fitting 2D Gaussian models to the combined image. The results from the model are given in Table 3.3.

The emission parallel and perpendicular to the major axis of the Gaussian fit was studied in order to determine whether the disc and jet of DG Tau B were resolved. The peak of the emission was assumed to be the position of DG Tau B. The emission from DG Tau B in 2014 was studied at angles of 112.7° and 22.7° . The emission in the 2016 epoch was studied at angles of 131.6° and 41.6° . The emission from the combined image was studied at angles of 114.0° and 24.0° . These angles were measured anticlockwise from north.

The emission was normalised to the peak intensity and each cross cut was fit with a Gaussian using the IDL routine *mpfitpeak*. The cross cuts for each epoch, as well as the combined observation are shown in Figures 3.5, 3.6 and 3.7. Cross cuts of the beam were also taken to determine the beam width parallel and perpendicular to the long axis of the source as well as the position angle. The results of these cross cuts for each observation can be found in Table 3.4. The beam widths were plotted onto the cross cuts of the emission of DG Tau B.

The FWHM of the emission along the minor axis of DG Tau B, as seen in Figure 3.5a, in 2014 is comparable with the size of the beam. Therefore, the structure is unresolved in this direction. The emission perpendicular to this has also been studied in Figure 3.5b. The emission along the major axis has a larger FWHM

CHAPTER 3

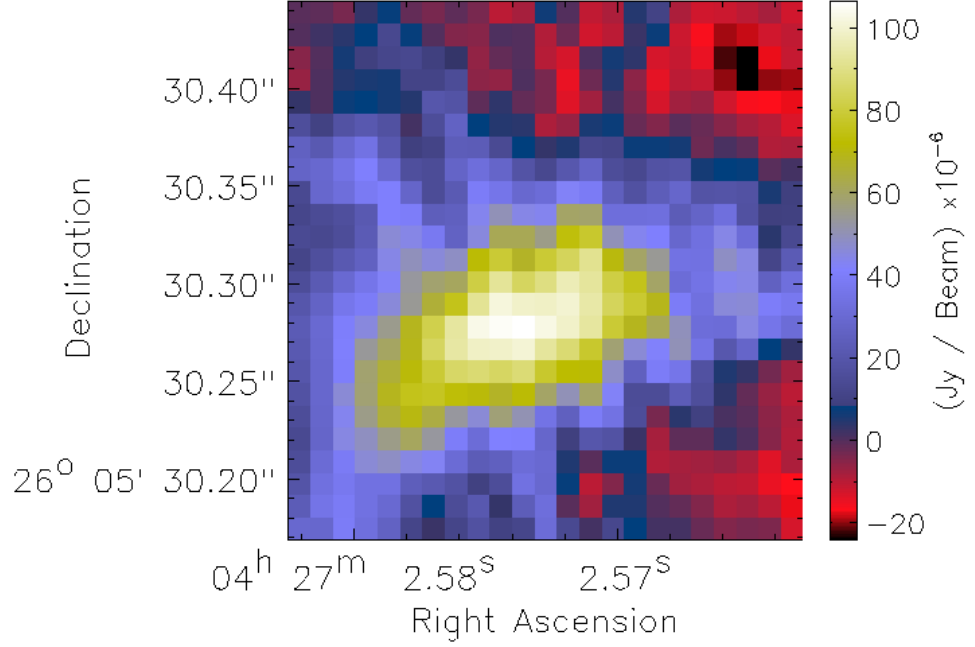
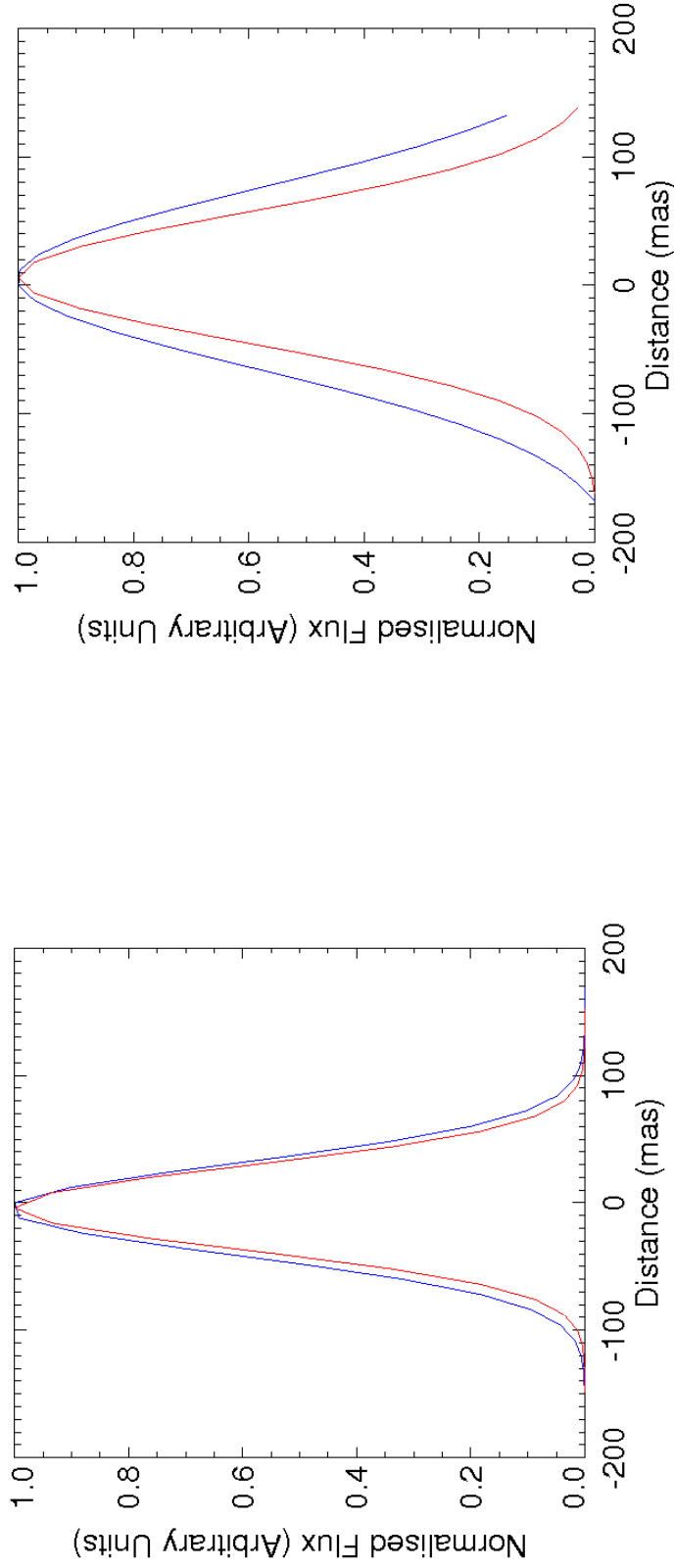


Figure 3.4: Image of DG Tau B made by combining and averaging the data from the 2014 and 2016 epoch. The observations were first aligned by assuming the position of the peak is due to DG Tau B. The 2016 epoch was then rotated to ensure the jet of DG Tau B was aligned in both epochs.

Table 3.4: Parameters of the beam in each epoch

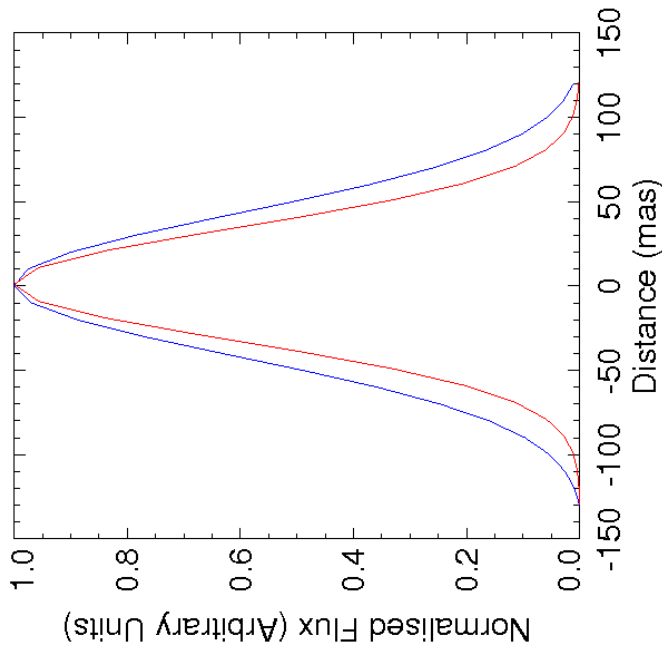
Epoch	Beam Major (mas)	Beam Minor (mas)	Beam Position Angle ($^{\circ}$)
2014	119.5	76.7	70.0
2016	120.0	80.0	68.0
Combined	119.8	78.4	70.0



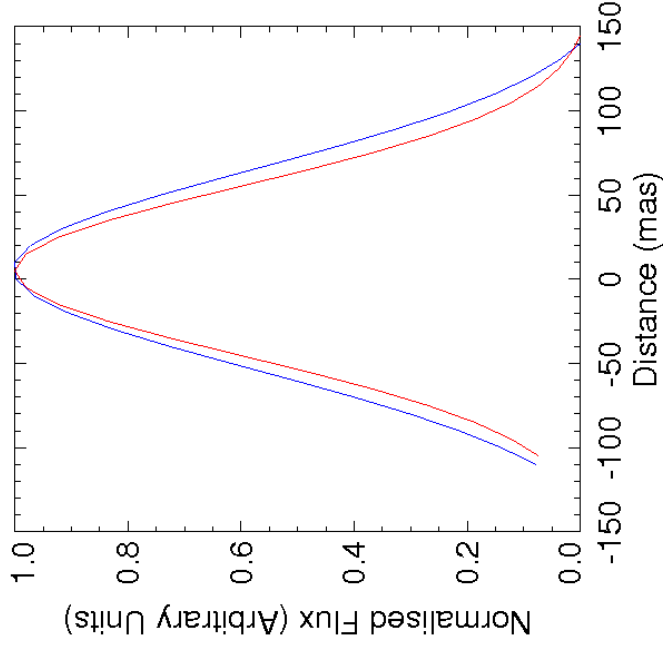
(a) The emission from DG Tau B along the minor axis of the Gaussian model. This cross cut has been made at an angle of 22.7° , measured anticlockwise from north.

(b) The emission from DG Tau B along the major axis of the gaussian model. This cross cut has been made at an angle of 112.7° , measured anticlockwise from north.

Figure 3.5: The emission from DG Tau B studied along the major and minor axis of the Gaussian model. The emission has been fit with a Gaussian and is shown in blue; the beam is shown in red. Observations used to make this cross cut were made in 2014.

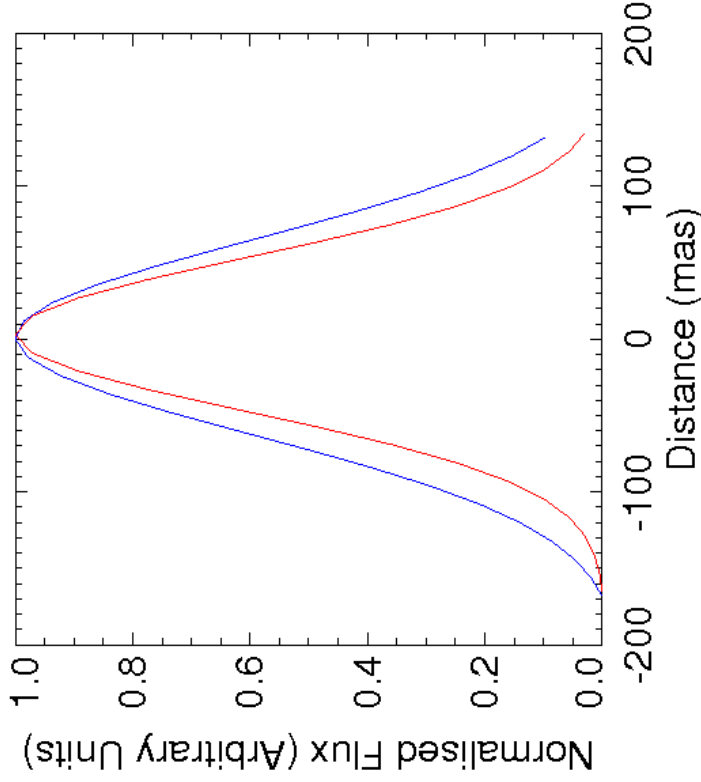


(a) The emission from DG Tau B along the minor axis of the Gaussian model. This cross cut has been made at an angle of 41.6° , measured anticlockwise from north.

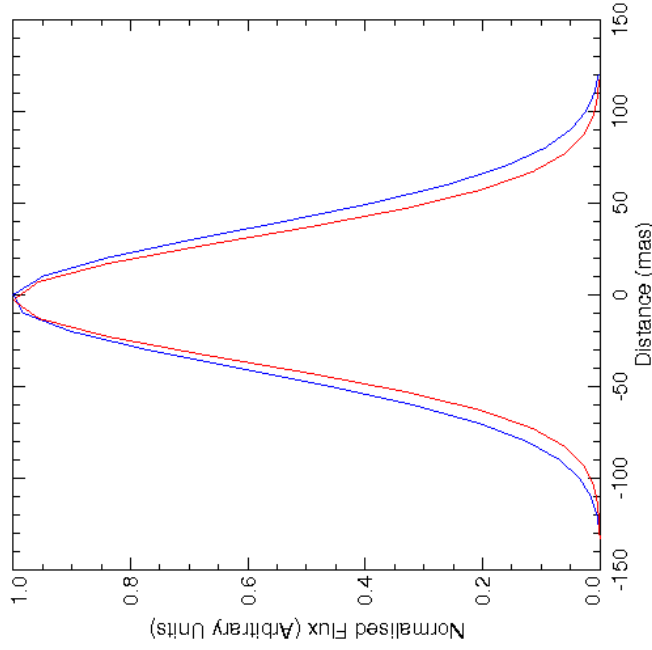


(b) The emission from DG Tau B along the major axis of the gaussian model. This cross cut has been made at an angle of 131.6° , measured anticlockwise from north.

Figure 3.6: The emission from DG Tau B studied along the major and minor axis of the Gaussian model. The emission has been fit with a Gaussian and is shown in blue; the beam is shown in red. Observations used to make this cross cut were made in 2016.



(a) The emission from DG Tau B along the major axis of the Gaussian model. This cross cut has been made at an angle of 114.0° , measured anticlockwise through north.



(b) The emission from DG Tau B along the minor axis of the Gaussian model. This cross cut has been made at an angle of 24.0° , measured anticlockwise from north.

Figure 3.7: The emission from DG Tau B studied along the major and minor axis of the Gaussian model. The emission has been fit with a Gaussian and is shown in blue; the beam is shown in red. This cross cut was made using the combined observations of DG Tau B in 2014 and 2016.

CHAPTER 3

than the size of the beam. Therefore, the structure along the major axis has been resolved.

The emission along the minor axis of the Gaussian fit in the 2016 epoch appears to have a slightly larger FWHM than that of the beam. Therefore, the emission that has been studied in Figure 3.6a is slightly resolved. The major axis which lies parallel to the direction of the DG Tau B jet has been studied in Figure 3.6b and the FWHM of the emission is larger than the beam. Therefore, the emission along both the major and minor axis of the Gaussian fit has been resolved in the 2016 epoch.

The cross cuts from the combined observation bare similar results to that of the 2016 e-MERLIN observation. The emission along the minor axis (Figure 3.7a) is only slightly resolved compared to the size of the beam. Whereas the emission that lies along the major axis is resolved (Figure 3.7b). Therefore, we conclude that the emission along the minor axis has only slightly been resolved with e-MERLIN, whilst the emission along the major axis has been resolved.

Chapter 4

A mm Study of DG Tau B

4.1 New Data : Observations with the EVLA

Observations of DG Tau B were conducted using the EVLA in 2010 at a frequency of 34.0 GHz (8.8 mm). The data were calibrated using *CASA* and a modified version of the EVLA calibration pipeline (see <https://science.nrao.edu/facilities/vla/data-processing/pipeline>). The pipeline performs basic flagging and calibration following the processes outlined in Section 2.2 .

The disc surrounding DG Tau B is unresolved at cm wavelengths and no cm size dust has been detected. A resolved disc at mm wavelengths would allow us to determine the upper limit on the grain size distribution in the disc surrounding DG Tau B.

The observation of DG Tau B can be seen in Figure 4.1. The beam for the observation is shown in the lower left and is $0.08 \times 0.07''$ with a position angle of -73.0° . The beam used in the EVLA observation is a near circular beam, whereas the e-MERLIN observations were taken using an elliptical beam. The position of DG Tau B lay nearly directly overhead during the EVLA observation which resulted in a near circular beam. Whereas, the position of DG Tau B during the e-MERLIN observation lay closer to the horizon. There are also significantly less residuals from

CHAPTER 4

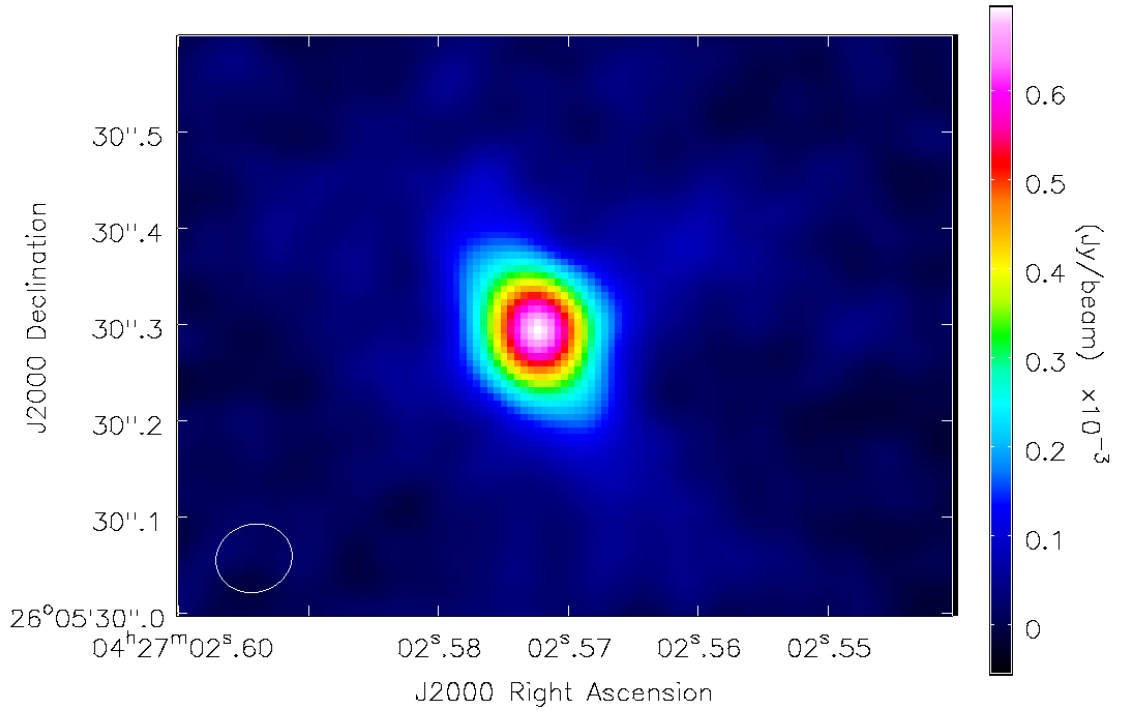


Figure 4.1: Observation of DG Tau B taken with the EVLA in 2010. The observations were taken at a frequency of 34.0 GHz (8.8 mm). The beam, in the lower left, is $0.08 \times 0.07''$ with a position angle of -73.0° .

the cleaning processes in the EVLA data than the e-MERLIN.

An elongated structure can be seen in the EVLA observation extending from NE to SW. The elongated structure in the EVLA observation lies perpendicular to the structure seen in the e-MERLIN observation. Following our assumption in Section 3.4 that the jet lies parallel to the major axis in the e-MERLIN observation, we assume that the elongated structure seen in Figure 4.1 is the protoplanetary disc surrounding DG Tau B.

The EVLA observations were studied following the method outlined in Section 3.2. A two-dimensional elliptical Gaussian was fit to DG Tau B to determine various parameters of the system. This was done using *imfit* in *CASA*. The results from this fit can be found in Table 4.1. At this epoch we found the position of DG Tau

CHAPTER 4

Table 4.1: Parameters of DG Tau B found by fitting elliptical Gaussians to the EVLA data.

Parameter	2010
RA (J2000) $+04^h27^m(s)$	02.5724 ± 0.0001
Dec (J2000) $+26^\circ05'(\prime)$	30.293 ± 0.002
Deconvolved Major Size (mas)	113.0 ± 7.0
Deconvolved Minor Size (mas)	71.4 ± 6.4
Position Angle ($^\circ$)	25.5 ± 6.8
Integrated Flux (mJy)	1.63 ± 0.09
Peak Flux ($\mu\text{Jy beam}^{-1}$)	643 ± 25
Frequency (GHz)	34.0

B to be $\alpha_{J2000.0} = +04^h27^m02.5724^s \pm 0.0001^s$, $\delta_{J2000.0} = +26^\circ05'30.293'' \pm 0.002''$. The EVLA observations were conducted four years prior to the first e-MERLIN observation and the position of DG Tau B has changed between the two epochs. This could be due to the proper motion of the system.

An integrated flux density and peak flux of DG Tau B were found to be 1.63 ± 0.09 mJy and $643 \pm 25 \mu\text{Jy beam}^{-1}$ respectively. The integrated flux was measured over the deconvolved size of DG Tau B which was determined to be $113.0 \times 71.4 \pm 7.0 \times 6.4$ mas with a position angle of $25.5 \pm 6.8^\circ$. Therefore, at the distance of the DG Tau B (150pc), we find the size of the continuum source to be $\approx 17 \times 11 \pm 1 \times 1$ AU. The integrated flux value was included in the SED of DG Tau B shown in Figure 3.3.

4.2 Cross Cut Analysis

Analysis of the emission of DG Tau B observed with the EVLA data was conducted following the method outlined in Section 3.4. The FWHM along the major and minor axis was first found. This was done by fitting 2D Gaussian models to the observations. The parameters from the model can be found in Table 4.2. The major axis of the Gaussian fit has a FWHM of 100.0 ± 0.6 mas whilst the minor axis has a FWHM of 78.8 ± 0.5 mas.

The major axis is aligned parallel to the elongated structure seen in the EVLA observation. The major axis has an angle of $28.4 \pm 2.0^\circ$ measured anticlockwise from north. Assuming that the disc is aligned to the major axis and the jet lies perpendicular to this, the jet is $118.4 \pm 0.8^\circ$ measured anticlockwise from north. This agrees with the change in jet angle found in the e-MERLIN data and further implies that either the jet is precessing, or it is an effect of the proper motion of the system.

The emission along the major and minor axis of the Gaussian model of DG Tau B was studied. This was done in order to determine if the DG Tau B disc and jet had been resolved or not. The location of the peak intensity was taken to be the position of DG Tau B. The emission from the EVLA observation of DG Tau B was studied at angles of 28.4° and 118.4° , measured anticlockwise from north.

The emission was normalised to the peak intensity and each cross cut was fit with a Gaussian using the IDL routine *mpfitpeak*. The cross cuts along the major and minor axis are shown in Figures 4.2a and 4.2b respectively. Cross cuts of the beam were also taken to determine the beam width parallel and perpendicular to the long axis of the source as well as the position angle. The beam of the EVLA observation has a size of 80×70 mas with a position angle of -73° . The beam was plotted onto the cross cuts of DG Tau B in order to determine if the emission has been resolved or not.

The FWHM of the emission along the major axis of DG Tau B, as seen in Figure

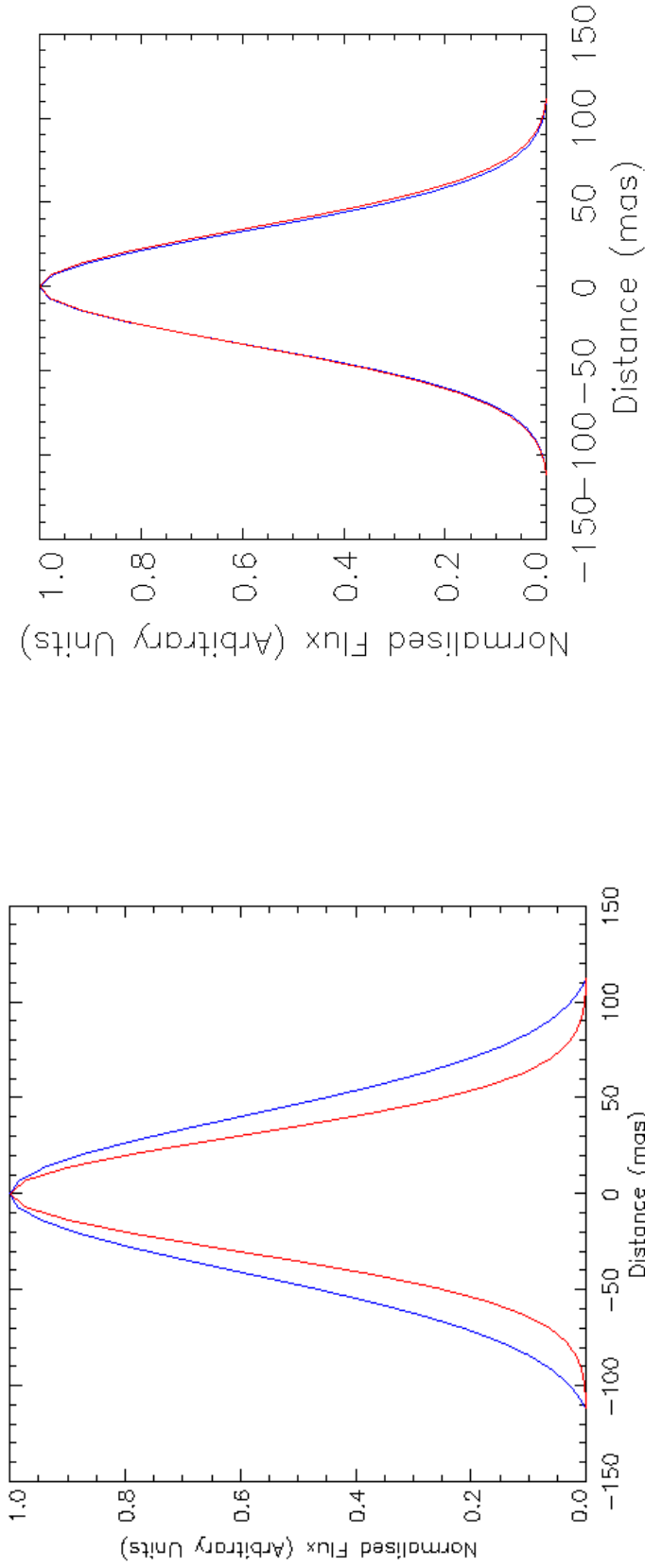
CHAPTER 4

4.2a, is larger than the size of the beam. Therefore, the structure is resolved in this direction. Perpendicular to this, the FWHM of the minor axis is comparable to the size of the beam. This can be seen in Figure 4.2b. Following our assumption that the disc lies parallel to the major axis in the EVLA data, we conclude that we have resolved the disc of DG Tau B at mm wavelengths but not the jet.

CHAPTER 4

Table 4.2: Parameters of DG Tau B found by fitting a 2D Gaussian model to the EVLA data. The angle of the major axis is measured anticlockwise from north.

Epoch	FWHM of Major Axis (mas)	FWHM of Minor Axis (mas)	Angle of Major Axis ($^{\circ}$)
2010	100.0 ± 0.6	78.8 ± 0.5	28.4 ± 2.0



(a) The emission from DG Tau B along the major axis of the Gaussian model. The cross cut has been made at an angle of 28.4° , measured anticlockwise from north.

(b) The emission from DG Tau B along the minor axis of the Gaussian model. The cross cut has been made at an angle of 118.4° , measured anticlockwise from north.

Figure 4.2: The emission from DG Tau B studied along the major and minor axis of the Gaussian model. The emission has been fit with a Gaussian and is shown in blue; the beam is shown in red. The beam has dimensions of 80×70 mas. Observations used to make this cross cut were made in 2010 using the EVLA.

Chapter 5

Discussion

Observations of the young stellar object DG Tau B were studied in this thesis. Centimetre observations were made using the interferometer e-MERLIN whilst observations at mm wavelengths were made using the EVLA. The e-MERLIN observations were taken in 2014 at 6.48GHz (4.63cm) and at 7.25GHz (4.14cm) in 2014. The EVLA observations were made in 2010 at 30.0GHz (8.8mm).

The observations of DG Tau B are shown in Figures 3.2 and 4.1. The observations were reduced using *CASA* following the methods outlined in Section 2.2. Data from the Lovell Telescope were not included in the final e-MERLIN observations due to a large quantity of systematic errors in the calibration data. As the Lovell is the largest telescope in the array, the sensitivity of the final observations were reduced. Residuals from the e-MERLIN cleaning process can still be seen in the final observations. Attempts were made to clean the data further, however this compromised the emission from DG Tau B. There are significantly less residuals from the cleaning process seen in the EVLA data.

An elongated structure can be seen in both the e-MERLIN and EVLA observations however, they appear to be perpendicular to each other. The structure in the e-MERLIN observations extend from the NW to SE whilst the structure observed with the EVLA extends from the NE to SW.

CHAPTER 5

The observations conducted in this thesis were compared to observations made by Zapata et al. (2015) (see Figure 3.1). This was done in order to identify the elongated structure seen in the three observations. The structure in the e-MERLIN data lies parallel to the molecular outflow and jet seen by Zapata et al. (2015). Therefore, we suspect that e-MERLIN has detected the jet and/or molecular outflow of DG Tau B.

The structure in the EVLA observations lies perpendicular to the structure in the e-MERLIN observation. We have assumed that protoplanetary discs lie perpendicular to outflows from YSOs such as jets and therefore suspect that the disc of DG Tau B has been detected using the EVLA. We confirm these results by fitting cross cuts of the observations in Section 3.4 and 4.2, the results of which shall be discussed in Section 5.3.

Two-dimensional elliptical Gaussian components were fit to DG Tau B in order to determine various parameters of the system. This was done for both the e-MERLIN and EVLA observations. The extent of the emission from DG Tau B was used to plot a SED, the results from which will be discussed in Section 5.1. The position of DG Tau B appears to have changed over the three epochs of observation. This could either be due to its proper motion, or its proximity to the classical T-Tauri star DG Tau A. This is further discussed in Section 5.5.

5.1 SED Fitting

Previous observations of DG Tau B have been conducted at near-infrared, submillimetre and centimetre wavelengths. Observations at mm and cm wavelengths were carried out in this thesis.

An integrated flux density of $204 \pm 26 \mu\text{Jy}$ over a deconvolved size of $133 \times 74 \pm 27 \times 18$ mas was detected from DG tau B in 2014. The deconvolved size has a position angle of $106 \pm 18^\circ$. Therefore, at the distance of the DG Tau B (150pc), we

CHAPTER 5

find the size of the continuum source to be $\approx 20 \times 11 \pm 4 \times 3$ AU. An integrated flux density of $158 \pm 23 \mu\text{Jy}$ was detected from DG Tau B in 2016 over a deconvolved size of $153 \times 83 \pm 32 \times 11$ mas with a position angle of $130 \pm 8^\circ$. This corresponds to a size of $\approx 23 \times 13 \pm 5 \times 2$ AU.

An integrated flux density of 1.63 ± 0.09 mJy over a deconvolved size of $113.0 \times 71.4 \pm 7.0 \times 6.4$ mas was detected from DG Tau B at mm wavelengths. The deconvolved size has a position angle of $25.5 \pm 6.8^\circ$. At the distance of the DG Tau B (150 pc), we find the size of the continuum source to be $\approx 17 \times 11 \pm 1 \times 1$ AU.

The observations were used to plot a spectral energy distribution of DG Tau B which can be seen in Figure 3.3. In order to model the thermal emission from the cold dust in the disc, a modified blackbody, described by Equation 1.5, was used. This allowed us to determine the mass and temperature of the dust in the disc surrounding DG Tau B.

This thesis is solely focussed on the circumstellar material in the protoplanetary disc, therefore, observations at wavelengths smaller than 100 microns were not modelled. Thermal emission at these smaller wavelengths is produced by hot dust closer towards the young stellar object (Dullemond et al. 2007) or from the YSO itself.

To fit the modified blackbody, we have adopted a distance to DG Tau B of 150 pc. This measurement is based upon previous parallax measurements conducted by Torres et al. (2007, 2012, 2009). Assuming a gas-to-dust ratio of 100:1, and following Beckwith et al. (1990), we use Equation 3.1 to determine the mass opacity coefficient, $\kappa_d(\nu)$. We adopt a value of $\beta = 1$ for the opacity spectral index based upon previous observations of protoplanetary discs (Beckwith & Sargent 1991, Andrews & Williams 2005).

The disc mass determined by fitting a modified greybody to the SED should be treated as a lower limit. This is due to a number of errors associated with this method of determining the disc mass.

CHAPTER 5

Firstly, DG Tau B is a Class I young stellar object and may still be embedded inside its infalling envelope. The contribution from dust in the envelope and the disc are hard to separate, therefore the emission detected from DG Tau B may be contaminated by emission from the surrounding envelope. This would affect the modified blackbody used to fit the SED and hence, the determined disc mass.

Secondly, we have assumed that the temperature of the dust grains is uniform across the disc. However, protoplanetary discs are rarely isothermal as gravitational instabilities in the disc can vary the local temperature (Evans et al. 2015). A change in the temperature of the disc results in a change of dust mass calculated using Equation 1.5. Therefore, by modelling the SED using one temperature, we may be neglecting some of the hotter dust found in the protoplanetary disc.

One of the biggest areas of uncertainty in the determination of the dust mass is the mass opacity coefficient. The opacity has a power-law dependence upon frequency according to $\kappa_d(\nu) \propto \nu^\beta$. The value of the opacity spectral index for a protoplanetary disc, β_{disc} , is still widely speculated. If we assume that the dust in a protoplanetary disc is both optically thin and similar to interstellar dust, we expect values of $\beta_{disc} \approx 2$ (Draine 2006). However, Beckwith & Sargent (1991) and Andrews & Williams (2005) both predict $\beta_{disc} \approx 1$ for protoplanetary discs. β_{disc} values of less than one have also been determined and these have been attributed to grain growth in the disc (Calvet et al. 2002, Testi et al. 2003).

There are a number of reasons as to why the value of β_{disc} varies across the literature. Assumptions that protoplanetary discs are optically thin are often made (including in this thesis). A disc may contain regions that are optically thick, affecting the true value of β_{disc} . The composition of the dust grains may also affect the value of β_{disc} . Spheroids of silicate or graphite will have $\beta \approx 2$ above $100\mu\text{m}$ whilst particles in a fractal arrangement have $\beta \lesssim 1$ beyond 1 mm (Beckwith et al. 1990).

Recent work by Dunham et al. (2014) and Evans et al. (2017) have shown that

CHAPTER 5

assuming the protoplanetary disc is isothermal and selecting an incorrect value for β_{disc} may result in disc mass underestimates by up to factors of 2-3 at millimetre wavelengths or up to an order of magnitude at smaller wavelengths.

The modified blackbody was fit to the SED using a mass of $M = 0.30 \pm 0.03 M_{\odot}$ and $T = 9.6 \pm 0.6 \text{K}$ respectively. Comparisons of results found in this thesis with other work shall be discussed in Section 5.2.

There is an excess of radiation seen at radio frequencies on the SED. The excess emission can be attributed to a number of mechanisms including thermal blackbody radiation from dust in the disc, free-free and synchrotron emission from the DG Tau B jet. The excess could also be due to a photoevaporative wind. In order to determine the source of the excess we calculated its spectral index, α .

The excess radiation at radio frequencies has been fit using a power law. The spectral index of the DG Tau B radio excess was calculated to be $\alpha = 1.4 \pm 0.2$. This spectral index is a combination of thermal greybody and free-free/synchrotron spectral indices. The spectral index due to thermal greybody radiation at radio wavelengths was found to be $\alpha_{greybody} = 3.0 \pm 0.1$. The difference between α and $\alpha_{greybody}$ is equal to the spectral index of the free-free/synchrotron emission. This was determined to be $\alpha_{free-free/sync} = 0.3 \pm 0.2$.

Draine (2006) showed that a spectral index of $2.0 < \alpha < 3.0$ is indicative of particles three times their observing wavelength. Dust grains that truncate at small sizes will have spectral indices of $\alpha > 3$. There have been a number of studies to determine the spectral index of the free-free and synchrotron emission produced by stellar winds and jets (Panagia & Felli 1975, Olon 1975, Wright & Barlow 1975 Reynolds 1986), and a spectral index range of $-0.1 < \alpha < 1.0$ was found.

The spectral index we have determined for DG Tau B agrees with the spectral index values attributed to free-free and synchrotron radiation. Therefore, we suspect that the radio excess is predominantly produced by the DG Tau B jet and/or stellar

wind rather than by dust grains in the protoplanetary disc.

5.2 Comparing the SED Results with Previous Observations

A disc mass estimate for the disc surrounding DG Tau B has previously been determined in Robitaille et al. (2007). They use a method first presented in Robitaille et al. (2006), to analyse the spectral energy distributions of Young Stellar Objects. The method fits the SED of YSOs using pre-computed two-dimensional Monte Carlo radiation transfer models. The fourteen model parameters varied for 20,000 models include stellar mass, radius and temperature, disc mass and radius, and envelope accretion rate for young objects. Each model has also been computed at 10 viewing angles, resulting in 200,000 SED models.

The models were tested on thirty young and spatially resolved sources in the Taurus-Auriga star-forming region (Robitaille et al. 2007). The disc surrounding DG Tau B was modelled using a mass of $0.074^{+0.259}_{-0.050} M_{\text{dot}}$. The disc mass determined in this thesis marginally agrees with the mass found in (Robitaille et al. 2007) within errors.

Robitaille et al. (2007) state that the disc masses determined for embedded sources like DG Tau B may not be well constrained. The uncertainty in the disc masses arise from reasons explained in Section 5.1.

The upper and lower limit for the disc mass and dust temperature that can be used to fit modified blackbodies to the SED is shown in Figure 5.1. The cold dust in the disc can be modelled using a temperature of 17K and mass of $0.13 \pm 0.1 M_{\odot}$. The dust in this model is warmer than the dust derived in the best fit model whilst the mass of the disc has decreased. The disc mass derived in this model agrees with the disc mass derived by Robitaille et al. (2007). The data can also be fit using a

temperature of 7K and mass of $0.53 \pm 0.1 M_{\odot}$. The dust in this model is colder whilst the mass of the disc has increased. The disc mass derived in this model however does not agree with the disc mass determined by Robitaille et al. (2007). To account for the full range of values seen, we adopt a disc mass of $0.3 \pm 0.3 M_{\odot}$.

5.3 Gaussian Fitting

The emission of DG Tau B detected with e-MERLIN and the EVLA has been studied by performing cross cuts on the observations. This determined if the jet and/or disc surrounding DG Tau B has been resolved or not.

Two-dimensional Gaussians were fit to the observations in order to determine the FWHM of the emission from DG Tau B. This was done in IDL using the routine *MPFIT2DPEAK*. The emission along the major and minor axis of the Gaussian fit was then studied. The emission was normalised to the peak intensity and each cross cut was fit using a Gaussian curve. In order to determine if the emission along the major and minor axis of DG Tau B had been resolved or not, the parameters of the beam in each epoch was found. The FWHM of the major and minor axis of the beam were then plotted onto each cross cut using the IDL routine *mpfitpeak*.

5.3.1 e-MERLIN Cross Cuts

The major axis of the Gaussian fit is aligned parallel to the elongated structure seen in Figures 3.2a and 3.2b, whilst the minor axis lay perpendicular to this. A FWHM of 156.7 ± 4.2 mas was determined for the major axis of DG Tau B in 2014 whilst the minor axis had a FWHM of 96.9 ± 2.6 mas. The angle of the major axis, measured anticlockwise from north was determined to be $112.7 \pm 4.6^{\circ}$. Following the assumption we have made above, that the elongated structure seen in the e-MERLIN observations lies parallel to the jet observed by Zapata et al. (2015), we

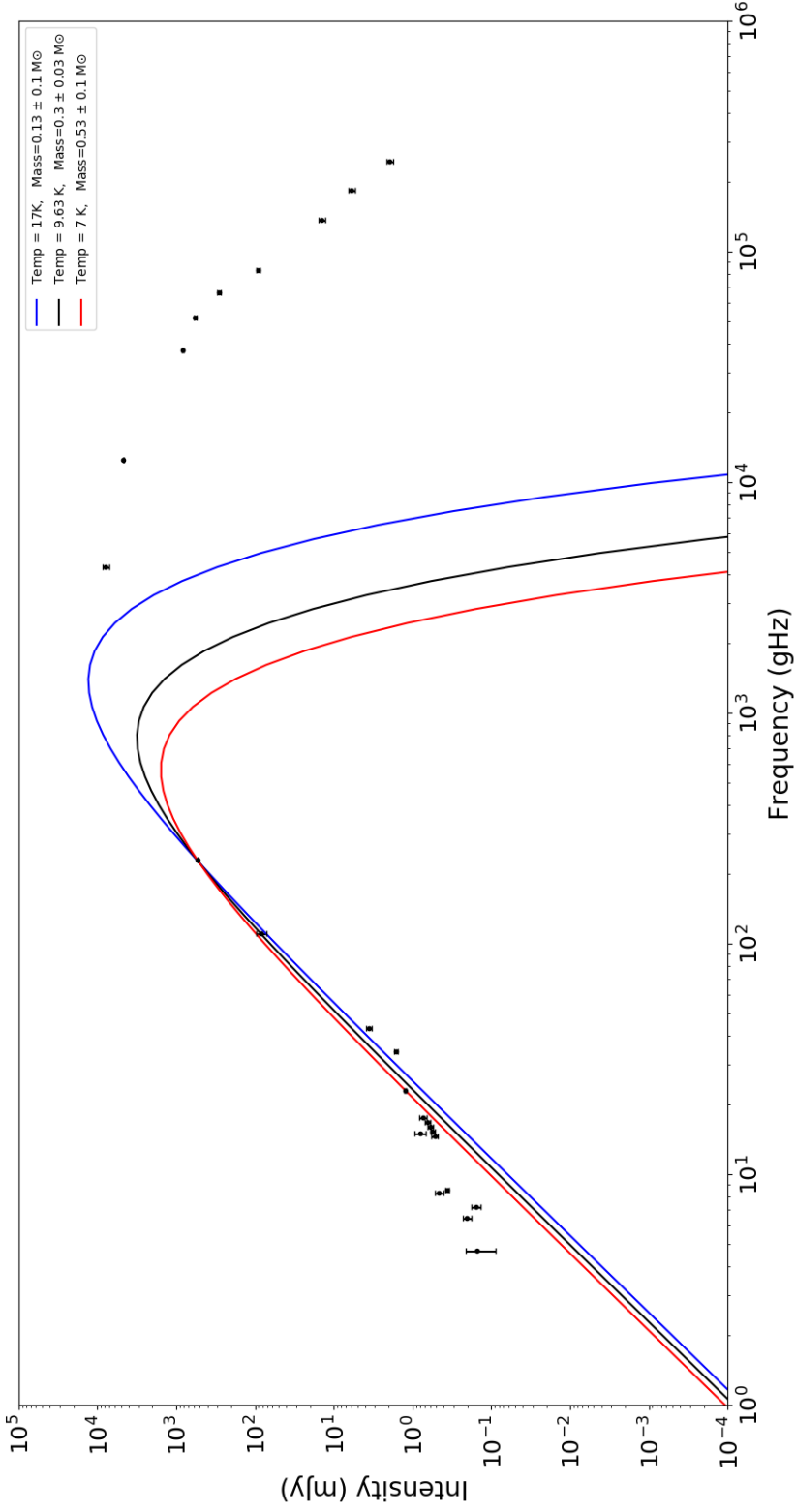


Figure 5.1: The cold dust in this SED of DG Tau B has been fit with the best fit model (black) as well as the upper and lower limit on the disc mass and temperature. The best fit (black) has been modelled with a a mass of $M = 0.30 \pm 0.03 M_{\odot}$ and temperature of $T = 9.63\text{K}$. The upper limit on the disc mass ($0.53 \pm 0.10 M_{\odot}$) has been modelled using a temperature of 7K (red). Whilst the lower limit on the disc mass ($0.13 \pm 0.10 M_{\odot}$) has been derived using a temperature of 17K (blue).

CHAPTER 5

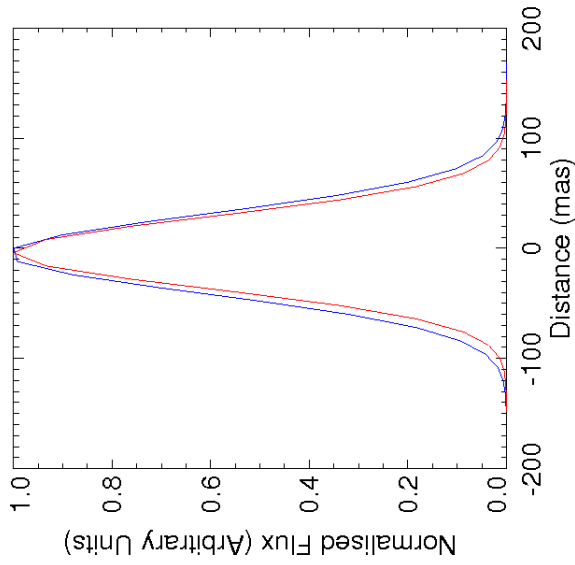
conclude that the angle of the jet is $112.7 \pm 4.6^\circ$, measured anticlockwise from north.

The emission from DG Tau B in 2014 was studied along angles of 22.7° and 112.7° , measured anticlockwise from north. The 2014 data were taken with a beam size of 119.5×76.7 mas with a position angle of 70.0° . The FWHM of the beam along an angle of 22.7° was plotted on the cross cut along the major axis of the Gaussian fit. The FWHM of the beam along an angle of 112.7° was plotted onto the cross cut along the minor axis of the Gaussian fit. The results of the 2014 e-MERLIN cross cuts are shown in Figures 5.2a and 5.2b.

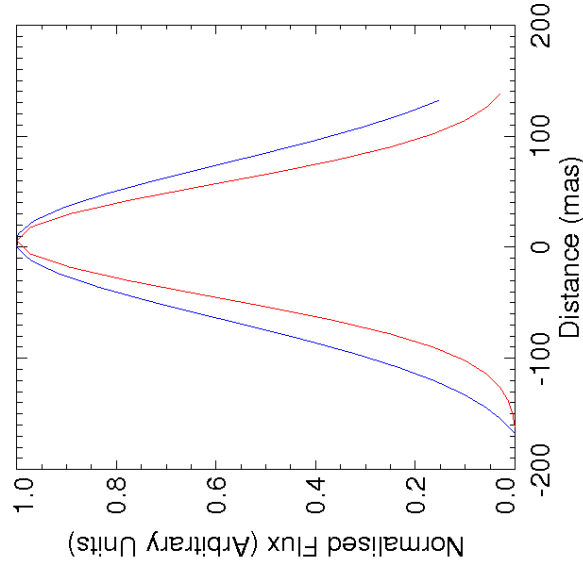
The FWHM of the emission along the minor axis is only slightly larger than the minor axis of the beam used in the observation. Therefore, the emission in this direction is unresolved. The emission parallel to the major axis has however, been resolved. The FWHM along the major axis of the beam is smaller than the FWHM of the emission from DG Tau B. Following our assumption that the major axis of the e-MERLIN observation is aligned parallel to the DG Tau B jet, we conclude that the disc surround DG Tau B in 2014 has not been resolved using e-MERLIN, however the jet has.

The FWHM of the major axis in the 2016 observation was determined to be 140.0 ± 5.0 mas, whilst the minor axis has a FWHM of 103.2 ± 2.5 mas. There is a decrease in the FWHM along the major axis between the two epochs, however, there is an increase along the minor axis. The angle, of what we assume is the jet of DG Tau B, was determined to be $131.6 \pm 3.4^\circ$ in the 2016 epoch. There is a difference of 18.9° between the angles of the jet in both epochs. This could be an effect of the proper motion of the system (discussed in Section 5.5 below), or the precession of the jet (discussed in Section 5.4).

Following the method explained above, the emission parallel and perpendicular to the major axis of the Gaussian fit of the 2016 e-MERLIN data was studied. The cross cuts for the 2016 data were made at angles of 41.6° and 131.6° , measured



(a) The emission from DG Tau B along the minor axis of the Gaussian model. This cross cut has been made at an angle of 22.7° , measured anticlockwise from north.



(b) The emission from DG Tau B along the major axis of the gaussian model. This cross cut has been made at an angle of 112.7° , measured anticlockwise from north.

Figure 5.2: The emission from DG Tau B studied along the major and minor axis of the Gaussian model. The emission has been fit with a Gaussian and is shown in blue; the beam is shown in red. Observations used to make this cross cut were made in 2014. This figure is a replica of Figure 3.5 and has been included for ease of reference.

CHAPTER 5

anticlockwise from north. The beam used to observe DG Tau B is 120.0×80.0 mas with a position angle of 68.0° . Cross cuts of the beam taken in the same direction as the 2016 cross cuts were made. These were then plotted onto the cross cuts of the emission from DG Tau B in the 2016 epoch, the results of which can be seen in Figures 5.3a and 5.3b. Unlike the 2014 observation of DG Tau B, both the minor and major axis have been resolved using e-MERLIN. Therefore, the jet and the emission perpendicular to this have been resolved.

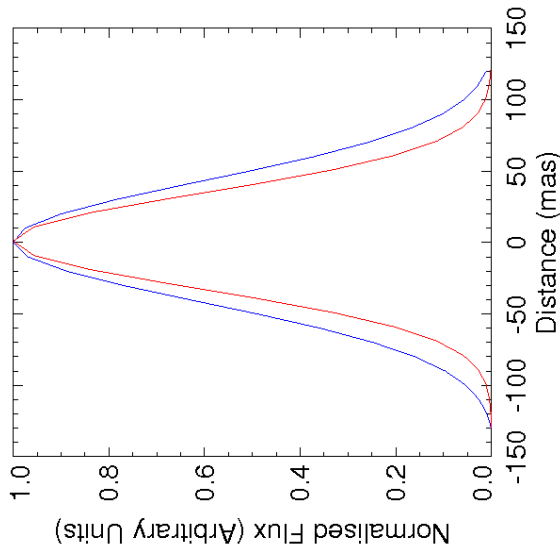
5.3.2 Combining Epochs

Upon first inspection of the data, the disc surrounding DG Tau B is not visible in Figures 3.2a and 3.2b. Therefore, the two epochs of data were combined. This was done to improve the signal to noise of the observation with the aim of improving the visible structure.

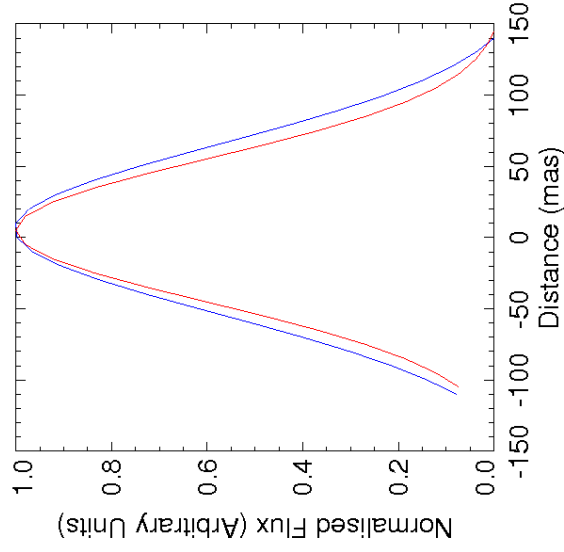
The position of the YSO had changed between the two epochs of observation, therefore the images were first aligned. The position of the peak emission was assumed to be the location of DG Tau B and the co-ordinates of this point were found. The difference between the peak position was determined and added onto the reference co-ordinate of the 2016 data. The 2014 data have a better signal to noise, therefore the 2016 data were aligned to the 2014.

The 2016 epoch of data was then rotated by an angle of 18.9° . This is to account for the rotation of the source between the two epochs of observation. Rotating one dataset relative to the other may blur the rotated data. This would affect the visible structure of the source as well as the detected emission.

There is a slight difference in frequency at which the observations were conducted (0.77GHz). We did not take this into account when combining and averaging the two epochs of data as the difference is so small. The combined data of DG Tau B are shown in Figure 3.4. There appears to be no significant improvement to the signal



(a) The emission from DG Tau B along the minor axis of the Gaussian model. This cross cut has been made at an angle of 41.6° , measured anticlockwise from north.



(b) The emission from DG Tau B along the major axis of the gaussian model. This cross cut has been made at an angle of 131.6° , measured anticlockwise from north.

Figure 5.3: The emission from DG Tau B studied along the major and minor axis of the Gaussian model. The emission has been fit with a Gaussian and is shown in blue; the beam is shown in red. Observations used to make this cross cut were made in 2016. This figure is a replica of Figure 3.6 and has been included for ease of reference.

CHAPTER 5

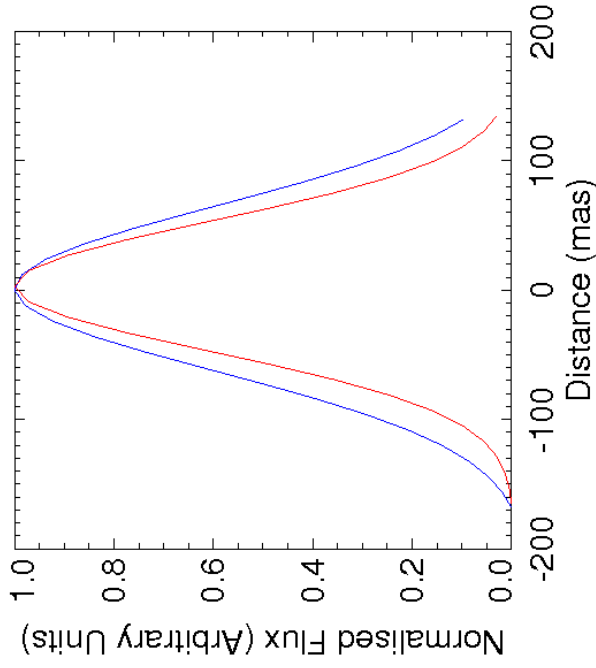
to noise of the structure parallel to the disc when compared to the 2014 and 2016 observations separately. The structure perpendicular to what we assume is the disc is more pronounced in the combined image than the 2014 and 2016 observations.

The FWHM of the major axis in the combined observation was determined to be 164.7 ± 7.3 mas. This is an increase from the FWHM values determined along the major axis of the Gaussian fit in the 2014 and 2016 epochs. The minor axis of the Gaussian fit to the combined image was found to have a FWHM of 90.5 ± 3.6 mas. The size of the beam for the combined observation is 119.8×78.4 mas with a position angle of 70.0° . Cross cuts of the emission were made following the method outlined above for the 2014 and 2016 observations, these are shown in Figures 5.4a and 5.4b. Similar to the 2016 epoch of the e-MERLIN observations, the emission both parallel and perpendicular to the major axis of the Gaussian fit has been resolved. However, the emission along the minor axis is only slightly resolved.

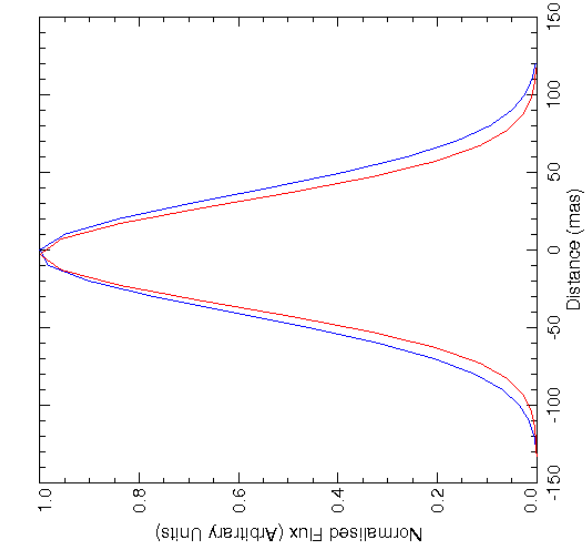
The emission along the major axis has been detected in both epochs of observation using e-MERLIN. It has also been resolved in the combined data. On the other hand, the emission along the minor axis has been unresolved in one epoch and only slightly resolved in another. We suspect that we have detected the jet of DG Tau B using e-MERLIN rather than the disc. Therefore, the main source of radio emission from the DG Tau B system can be attributed to free-free or synchrotron radiation rather than thermal blackbody radiation.

The lack of cm thermal blackbody radiation at cm wavelengths implies that there are no cm sized dust grains, or pebbles, in the disc surrounding DG Tau B. This is supported by the results of the SED modelling which showed that radio excess could be attributed to free-free and synchrotron radiation rather than thermal greybody radiation.

DG Tau B has previously been modelled as a Class I Young Stellar Object Luhman et al. (2010) that may still be embedded in an envelope (Robitaille et al.



(a) The emission from DG Tau B along the minor axis of the Gaussian model. This cross cut has been made at an angle of 24.0° , measured anticlockwise from north.



(b) The emission from DG Tau B along the major axis of the gaussian model. This cross cut has been made at an angle of 114.0° , measured anticlockwise through north.

Figure 5.4: The emission from DG Tau B studied along the major and minor axis of the Gaussian model. The emission has been fit with a Gaussian and is shown in blue; the beam is shown in red. This cross cut was made using the combined observations of DG Tau B in 2014 and 2016. This figure is a replica of Figure 3.7 and has been included for ease of reference.

CHAPTER 5

2007). Although its age has not been determined, Class I Young Stellar Objects are no older than a few hundred thousand years (Adams et al. 1987, Hartmann 1998). The lack of thermal emission at cm wavelengths may imply that this disc is too young to be forming cm sized dust grains.

The lack of thermal blackbody radiation in the disc of DG Tau B may also be explained by the presence of the DG Tau B jet and molecular outflow. The jet and molecular outflow of DG Tau B both emit free-free and/or synchrotron radiation at cm wavelengths. The jet of DG Tau B is extremely powerful and extends for up to 55" in some places (Mundt et al. 1991, Eisloffel & Mundt 1998) whilst the molecular outflow extends for approximately 40". If there are cm sized dust grains in the disc surrounding DG Tau B, and the disc has a small radius, it may not be possible to disentangle the emission due to the jet, molecular outflow and dust grains.

5.3.3 EVLA Cross Cuts

DG Tau B has also been studied at mm wavelengths. Cross cuts were also made to the EVLA observations following the method outlined above.

The major axis of the Gaussian model is aligned parallel to the elongated structure seen in Figure 4.1. This lies perpendicular to the major axis of the e-MERLIN observations. The FWHM along the major axis of the Gaussian fit was determined to be 100.0 ± 0.6 mas whilst 78.8 ± 0.5 mas is the FWHM along the minor axis of the Gaussian fit. The major axis has an angle of $28.4 \pm 2.0^\circ$ measured anticlockwise from north.

Cross cuts of the emission from DG Tau B were made at angles of 28.4° and 118.4° along the major and minor axis of the Gaussian fit. The emission was normalised to the peak and the FWHM of the beam along the same directions as the cross cuts were also found. These were plotted onto the cross cuts of the DG Tau B emission detected with the EVLA. The beam used in the EVLA observations is 80×70 mas.

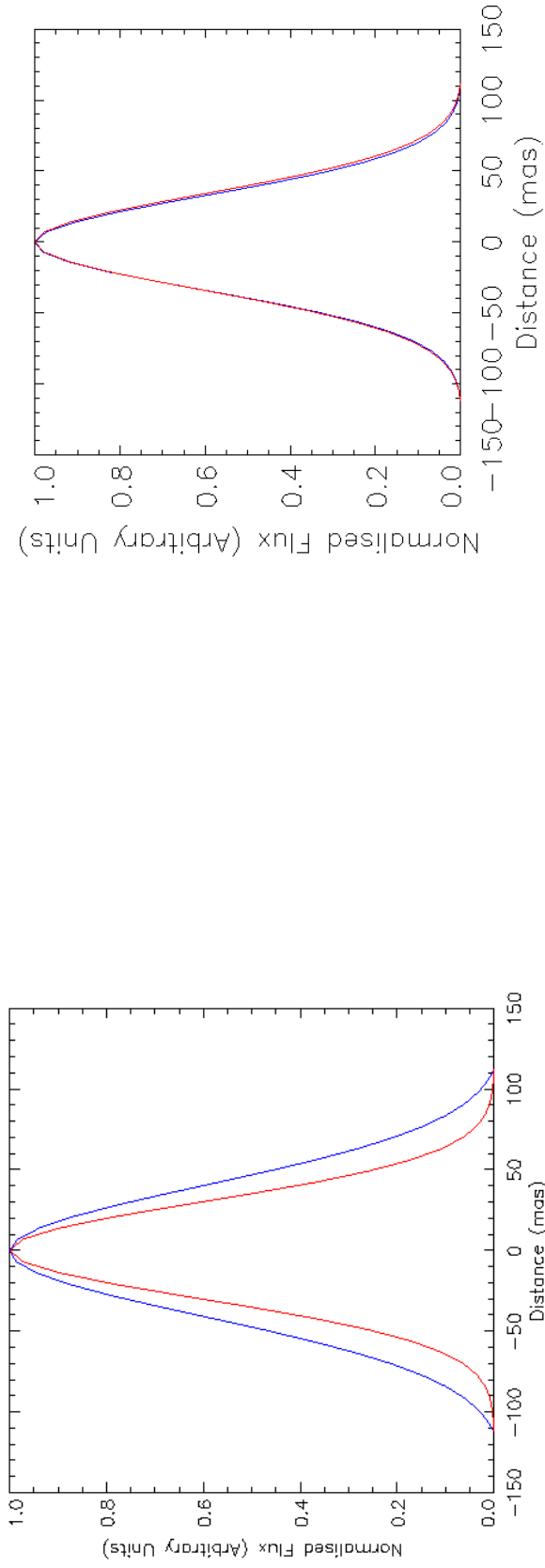
CHAPTER 5

The major axis of the beam is aligned parallel to the minor axis of the Gaussian fit and vice versa. The results from the EVLA cross cuts can be seen in Figures 5.5a and 5.5b.

The emission along the minor axis of the Gaussian fit of DG Tau B is unresolved. The FWHM is comparable with the size of the beam. Perpendicular to this, the emission is resolved. The FWHM of the emission along the major axis of the Gaussian fit is larger than the size of the beam. We have assumed that the elongated structure in the e-MERLIN observations is the DG Tau B jet. The major axis of the EVLA observations lies perpendicular to this, therefore, we suspect that the disc surrounding DG Tau B has been resolved with the EVLA.

The elongated structure seen in the EVLA observations may be an indication that a disc has been detected around DG Tau B. The detection of thermal blackbody radiation from the disc of DG Tau B at mm wavelengths may imply that there are mm sized dust grains in the disc, or it may simply be indicative of the dust temperature in the disc. The emission perpendicular to the disc is also unresolved which means that there is no contamination from the jet of DG Tau B.

The detection of mm thermal blackbody radiation, as well as the lack of cm blackbody emission detected with e-MERLIN, may provide an upper limit on the grain size distribution in the disc of DG Tau B. Cm sized dust grains have previously been detected in YSOs (Testi et al. 2003, Wilner et al. 2005, Rodmann et al. 2006, Lommen et al. 2009), however, the protostars in these studies have all been Class II YSOs(classical T-Tauri stars). The presence of mm emission but not cm emission may indicate that DG Tau B, a Class I YSO, may be too young to begin the formation of cm sized dust grains.



(a) The emission from DG Tau B along the major axis of the Gaussian model. The cross cut has been made at an angle of 28.4° , measured anticlockwise from north.

(b) The emission from DG Tau B along the minor axis of the Gaussian model. The cross cut has been made at an angle of 118.4° , measured anticlockwise from north.

Figure 5.5: The emission from DG Tau B studied along the major and minor axis of the Gaussian model. The emission has been fit with a Gaussian and is shown in blue; the beam is shown in red. The beam has dimensions of 80×70 mas. Observations used to make this cross cut were made in 2010 using the EVLA. This figure is a replica of Figure 4.2 and has been included for ease of reference.

5.4 DG Tau B Jet

Analysis of the DG Tau B SED revealed that the excess emission at radio wavelengths is primarily due to free-free or non-thermal emission. Both these mechanisms can explain the shallow spectral index determined for the radio excess.

Free-free emission from DG Tau B may arise from three sources. Photoevaporation of gas in the disc may contribute to the free free emission as well as ionised particles in the jet. Ambient gas surrounding the YSO being swept up by the fast moving jet causes a molecular outflow to be formed. Ionised gas from this outflow may be a source of the free-free emission being detected from DG Tau B. The non-thermal emission that may contribute to the radio excess seen on the SED may be from DG Tau B itself.

In order to locate the source of the radio excess, the e-MERLIN observations were compared to observations made by Zapata et al. (2015). The elongated structure seen in the e-MERLIN observations is resolved in both epochs and combined observation. It lies parallel to the jet and molecular outflow detected by Zapata et al. (2015). Therefore, we suggest that we have detected the jet and/or molecular outflow of DG Tau B, and it is these two components of the system primarily producing the free-free emission seen in the radio excess of the SED.

We have assumed that the major axis of the Gaussian model fit in Section 3.4 lies parallel to the DG Tau B jet. The angle of the major axis in 2014 was determined to be $112.7 \pm 4.6^\circ$ and $131.6 \pm 3.4^\circ$, therefore the angle of the jet has changed by 18.9° between the two observations. This could either be due to the proper motion of the DG Tau B system (discussed in Section 5.5) or the precession of the DG Tau B jet.

The precession of a jet indicates the change in its launching position. This may be caused by a change in the orientation of the accretion disc. Precessing jets have previously been detected emanating from Young Stellar Objects (Terquem et al. 1999, Bate et al. 2000). However these systems contain Classical T-Tauri stars in

CHAPTER 5

binary orbits rather than Class I young stellar objects such as DG Tau B.

Circumstellar jets trace emission ejected from the system on timescales < 10 years (Anglada et al. 2015). Molecular outflows on the other hand, trace emission ejected on timescales several orders of magnitude longer (Carrasco-González et al. 2008, López et al. 2006, 2015). Therefore, studying and comparing the ejection direction of the DG Tau B jet and molecular outflow may enable us to determine if the change in jet direction is due to precession or the proper motion of the system.

Previous observations of the jet of DG Tau B have been made in 1991 and 2004 ((Mundt et al. 1991) and McGroarty & Ray 2004). These studies found the angle of the jet to be 122° and 116° respectively. As well as this, the molecular outflow from DG Tau B has previously been detected with a principle angle of 114° . Infrared observations conducted by McGroarty & Ray (2004) reveal that there are several Herbig-Haro objects associated with DG Tau B. Each of these are well aligned with the DG Tau B jet which could mean that they are tracing ejecta from the YSO that took place thousands of years ago. The alignment of the jet, molecular outflow and Herbig-Haro objects detected across several epochs and studies indicate that the jet of DG Tau B may not be precessing.

There is a difference of almost 20° between the angle of the DG Tau B jet determined in 2016 compared with the jet angles found in both this work and literature. If the jet of DG Tau B is not precessing (for reasons outlined above), there may be another explanation for the change in angle measured for the DG Tau B jet. The 2016 e-MERLIN observations feature more residuals from the e-MERLIN cleaning process than the 2014 observations. Structure from the source may have been lost during the cleaning process which has resulted in a change in angle being measured for the DG Tau B jet.

5.5 Is DG Tau A and B A Binary?

Located at approximately 1' NW of DG Tau B is the classical T Tauri star DG Tau A. DG Tau A has been studied in greater depth than DG Tau B across various wavelengths (Isella et al. 2010, Podio et al. 2012, Ainsworth et al. 2013, Schneider et al. 2013), and it was one of the first T Tauri stars to be associated with an optical jet (Mundt & Fried 1983), which has since been found to extend for ≈ 0.5 pc (McGroarty et al. 2007). Observations of DG Tau A at mm wavelengths provide evidence for a disc surrounding the YSO containing mm sized dust grains (Beckwith et al. 1990, Kitamura et al. 1996, Dutrey et al. 1996, Rodmann et al. 2006).

DG Tau A and DG Tau B are thought to be unrelated except by projected proximity (Jones & Cohen 1986). The emission from DG Tau A may contaminate the sub-mm and mm emission detected by DG Tau B (AMI Consortium et al. 2012); this may provide an explanation as to why the sub-mm and mm SED of DG Tau B is poorly constrained. In order to determine if both YSOs are locked in a binary system, we intend to investigate the proper motion of both objects.

Along with DG Tau B, the disc surrounding DG Tau A has been studied as part of the Disks@EVLA and PEBBLEs surveys. Both these surveys aim to detect large dust grains in the disc surrounding DG Tau A. The observations with the EVLA and e-MERLIN were taken at the same frequency and epoch as the DG Tau B observations. The observations of DG Tau A were reduced and cleaned following the method outlined in Sections 3.2 and 4.1.

The position of DG Tau A and B in the e-MERLIN and EVLA observations were found by fitting two-dimensional elliptical Gaussian components to the data. This was done in *CASA* using *imfit*. We have assumed here that the peak emission is the location of DG Tau A and B in all observations. The positions of DG Tau A and B detected in previous observations as well as the positions determined in this thesis can be found in Tables 5.1 and 5.2.

CHAPTER 5

Table 5.1: Positions of DG Tau A used to investigate the proper motion of the system.

Epoch	RA (J2000) $04^h27^m(s)$	Dec (J2000) $+26^\circ06'(\prime\prime)$	Reference
1981	4.683 ± 0.006	16.35 ± 0.095	(1)
1984	4.676 ± 0.003	16.38 ± 0.01	(1)
1985	4.675 ± 0.003	16.23 ± 0.03	(1)
1994	4.687 ± 0.002	16.15 ± 0.01	(1)
1997	4.690 ± 0.001	16.12 ± 0.03	(1)
2010	04.697 ± 0.001	16.11 ± 0.01	(2)
2011	04.693	15.82	(3)
2014	04.700 ± 0.001	15.714 ± 0.002	(4)
2016	04.702 ± 0.001	15.677 ± 0.009	(4)

References. (1) Rodríguez, González, Raga, Cantó, Riera, Loinard, Dzib & Zapata (2012), (2) Disks@EVLA Chandler (2017), (3) Ainsworth et al. (2013), (4) PEBBLEs Greaves (2017)

The variation in the position of DG Tau A was studied first. The right ascension as a function of time is shown in Figure 5.6a whilst the declination is shown in Figure 5.6b. The Python package *curvefit* was used to add a least squares fit to the change in position of DG Tau A. This was done for both the right ascension and declination.

The gradient of the fits in Figures 5.6a and 5.6b were taken as the proper motion of DG Tau A. In order to calculate the proper motion of the right ascension in milliarcseconds, the declination between the first and last epoch in Table 5.1 was used. The proper motion of DG Tau A was determined to be:

$$\mu_{\alpha_a} \cos \delta = +8.95 \pm 1.40 \text{ mas yr}^{-1}$$

CHAPTER 5

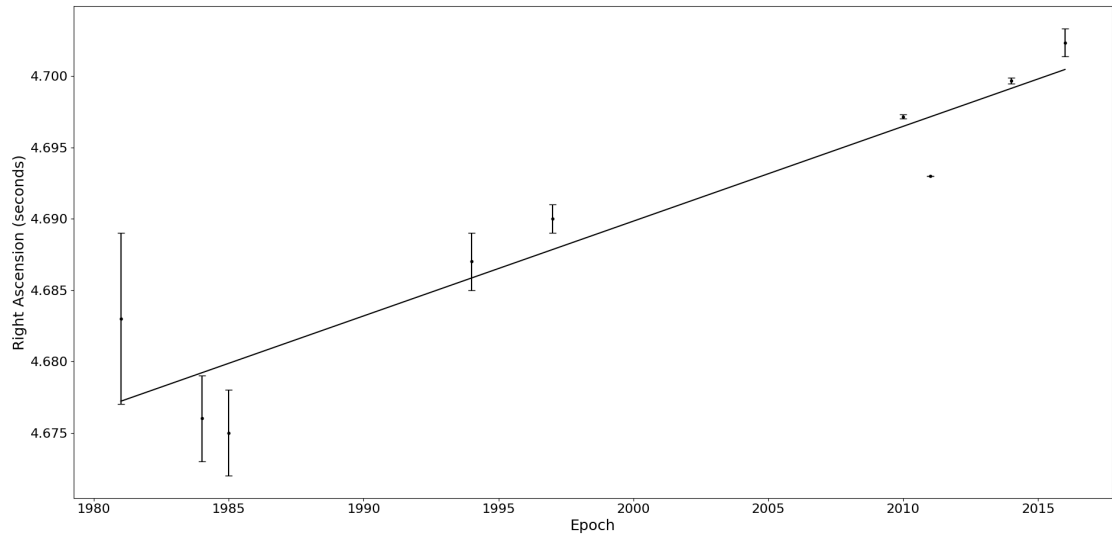
Table 5.2: Positions of DG Tau B used to investigate the proper motion of the system.

Epoch	RA (J2000) $04^h 27^m (s)$	Dec (J2000) $+26^\circ 05' (")$	Reference
1994	02.556 ± 0.003	30.65 ± 0.05	(1)
1997	02.561 ± 0.004	30.63 ± 0.06	(1)
2009	02.558 ± 0.002	30.22 ± 0.04	(1)
2010	02.572 ± 0.001	30.293 ± 0.002	(2)
2011	02.564 ± 0.002	30.38 ± 0.05	(1)
2014	02.574 ± 0.001	30.274 ± 0.004	(2)
2016	02.576 ± 0.001	30.211 ± 0.005	(2)

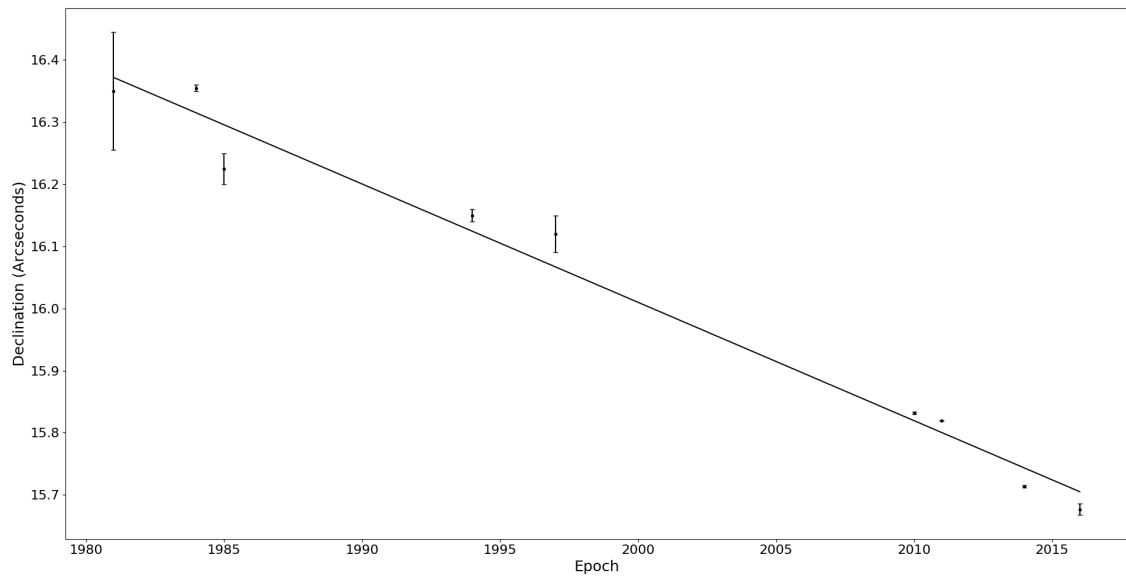
References. (1) Rodríguez, González, Raga, Cantó, Riera, Loinard, Dzib & Zapata (2012), (2)

This work

CHAPTER 5



(a) The right ascension of DG Tau A is given with respect to 04^h27^m



(b) The declination of DG Tau A is given with respect to $+26^{\circ}06'$

Figure 5.6: The right ascension (a) and declination (b) of DG Tau A over a 35 year period. The straight lines are least squares fits to the data that give the proper motions discussed in the text.

CHAPTER 5

$$\mu_{\delta_a} = -19.05 \pm 1.08 \text{ mas yr}^{-1}$$

A similar analysis was performed for DG Tau B. There are fewer position measurements for DG Tau B than A as it is a heavily obscured object and high resolution imaging is needed to determine its position. The variation in right ascension for DG Tau B is shown in Figure 5.7a. The declination variation is shown in Figure 5.7b. A least squares fit was also added to the DG Tau B data in order to determine its proper motion.

The declination between the first and last epoch in Table 5.2 was used to calculate the proper motion of the right ascension of DG Tau B in milliarcseconds. The proper motion of DG Tau B was determined to be:

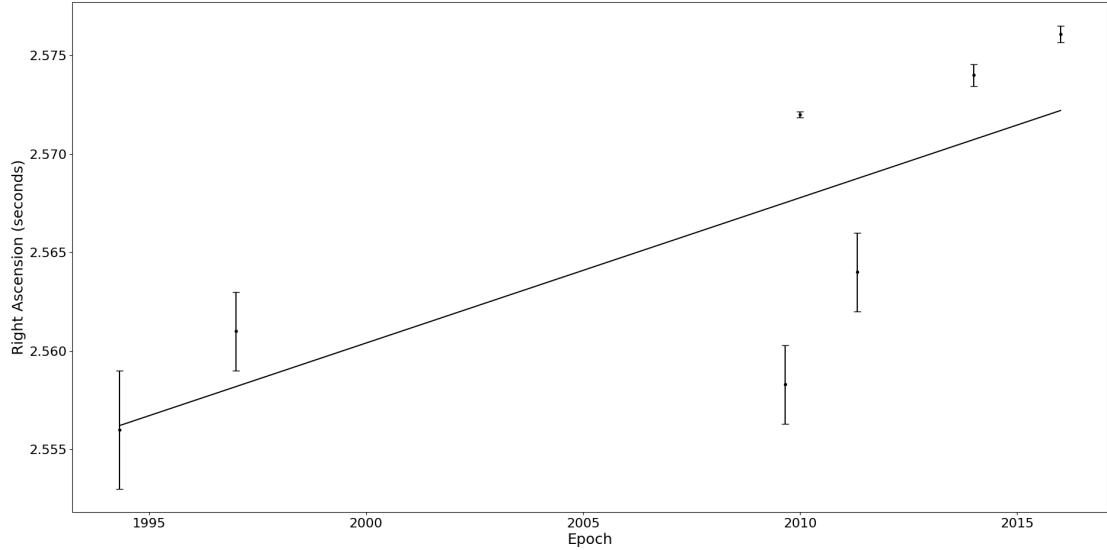
$$\begin{aligned}\mu_{\alpha_b} \cos \delta &= +9.94 \pm 4.11 \text{ mas yr}^{-1} \\ \mu_{\delta_b} &= -21.00 \pm 3.30 \text{ mas yr}^{-1}\end{aligned}$$

5.6 Comparing the Proper Motions to Previous Results

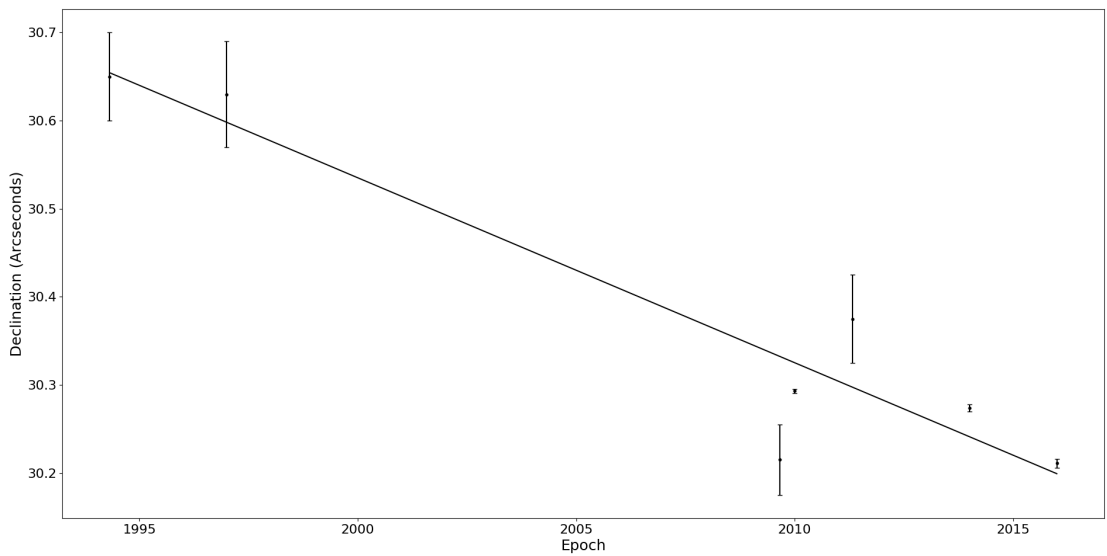
Rodríguez, González, Raga, Cantó, Riera, Loinard, Dzib & Zapata (2012) studied the continuum emission from DG Tau A using the Very Large Array (VLA) as well as determining its proper motion. The full set of observations used to calculate the proper motion of DG Tau A spans approximately 30 years and was determined to be: $\mu_{\alpha_a} \cos \delta = +7.5 \pm 0.9 \text{ mas yr}^{-1}$ and $\mu_{\delta_a} = -19.0 \pm 0.9 \text{ mas yr}^{-1}$.

The proper motion determined for DG Tau A in this work agrees with the proper motion determined in Rodríguez, González, Raga, Cantó, Riera, Loinard, Dzib & Zapata (2012). They are also consistent within $2\text{-}\sigma$ with the proper motion reported by Ducourant et al. (2005) ($\mu_{\alpha_a} \cos \delta = +3.0 \pm 2.0 \text{ mas yr}^{-1}$ and $\mu_{\delta_a} = -24.0 \pm 2.0 \text{ mas yr}^{-1}$) based upon optical observations.

CHAPTER 5



(a) The right ascension of DG Tau B is given with respect to $04^h 27^m$



(b) The declination of DG Tau B is given with respect to $+26^{\circ}05'$

Figure 5.7: The right ascension (a) and declination (b) of DG Tau B over a 22 year period. The straight lines are least squares fits to the data that give the proper motions discussed in the text.

CHAPTER 5

The continuum emission of DG Tau B has previously been studied by Rodríguez, Dzib, Loinard, Zapata, Raga, Cantó & Riera (2012) using the VLA. The proper motion of DG Tau B was determined to be: $\mu_{\alpha_b} \cos \delta = +3.8 \pm 1.9 \text{ mas yr}^{-1}$ and $\mu_{\delta_b} = -20.6 \pm 3.3 \text{ mas yr}^{-1}$. The proper motion of the declination is consistent with the proper motion derived by Rodríguez, Dzib, Loinard, Zapata, Raga, Cantó & Riera (2012), whilst the proper motion of the right ascension is only consistent within $2\text{-}\sigma$.

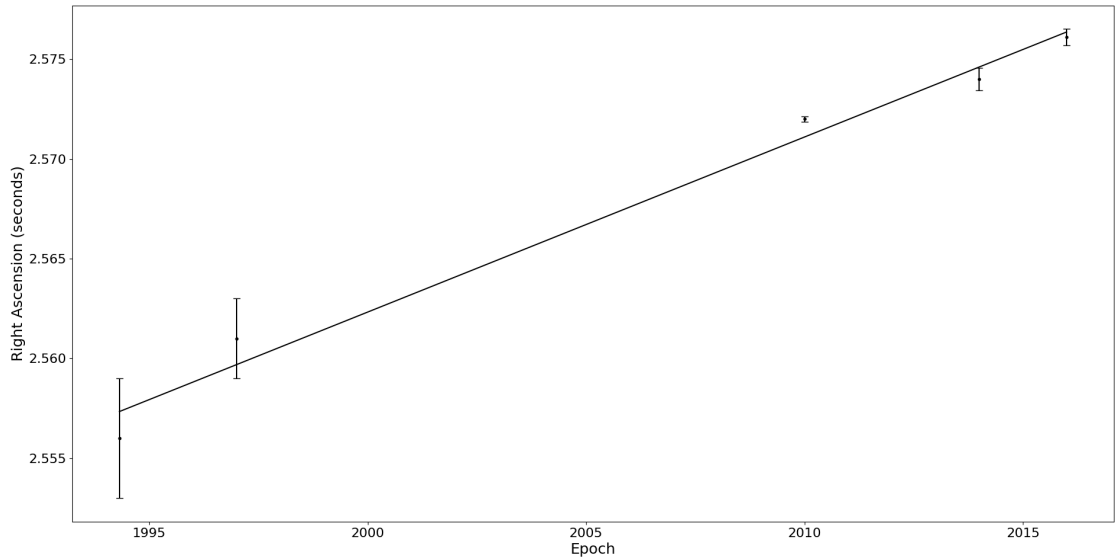
The position of DG Tau B detected by Rodríguez, Dzib, Loinard, Zapata, Raga, Cantó & Riera (2012) using the VLA in 2009 and 2011 do not lie close to the line of best fit plotted in Figures 5.7a and 5.7b. Therefore, the proper motion analysis was repeated without these two observations in order to investigate their significance on the final proper motion values. The position of DG Tau B across the 22 year period without the two VLA observations are shown in Figures 5.8a and 5.8b.

The proper motions of DG Tau B calculated using the new least squares fits were determined to be:

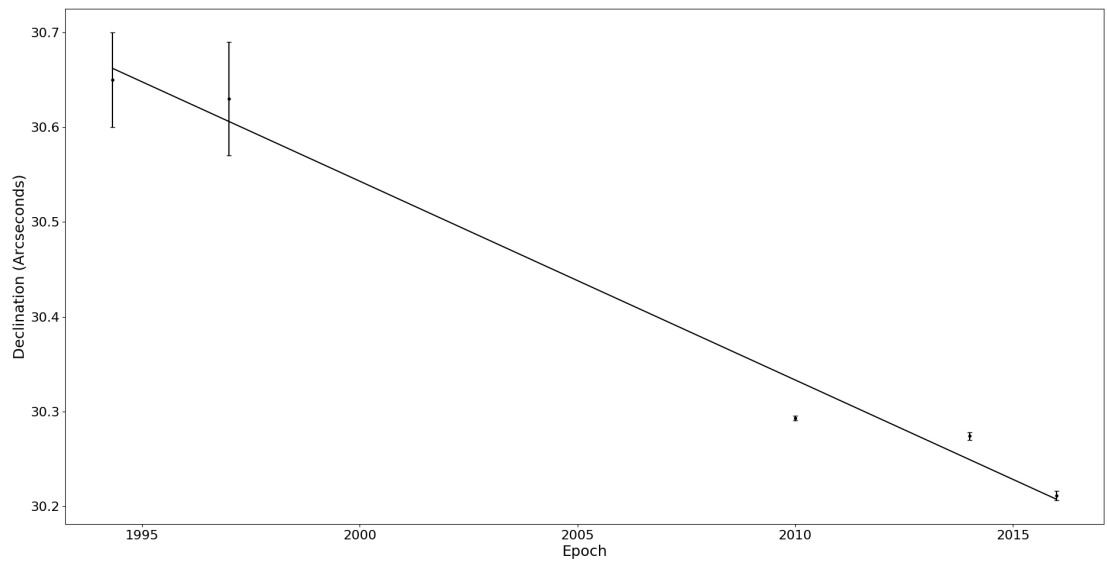
$$\begin{aligned}\mu_{\alpha_b} \cos \delta &= +11.81 \pm 0.95 \text{ mas yr}^{-1} \\ \mu_{\delta_b} &= -20.98 \pm 1.58 \text{ mas yr}^{-1}\end{aligned}$$

The removal of the VLA data has decreased the proper motion detected for the declination of DG Tau B. The new value is fractionally more consistent with the declination proper motion determined by Rodríguez, Dzib, Loinard, Zapata, Raga, Cantó & Riera (2012). However, the right ascension proper motion has increased, making it less consistent with Rodríguez, Dzib, Loinard, Zapata, Raga, Cantó & Riera (2012). The error measurement on both proper motion values has decreased, therefore, the proper motion determined without the VLA data has a greater degree of accuracy than the original results. These results are outlined in Table 5.3.

CHAPTER 5



(a) The right ascension of DG Tau B is given with respect to $04^h 27^m$



(b) The declination of DG Tau B is given with respect to $+26^\circ 05'$

Figure 5.8: The right ascension (a) and declination (b) of DG Tau B over a 22 year period. The data used to generate these plots does not include the two VLA observations conducted by Rodríguez, Dzib, Loinard, Zapata, Raga, Cantó & Riera (2012) in 2009 and 2011. The straight lines are least squares fits to the data that give the proper motions discussed in the text.

Table 5.3: The proper motions of DG Tau A and B derived in this thesis as well as from the literature

	$\mu_{\alpha_b} \cos \delta$ mas yr^{-1}	μ_{δ_b} mas yr^{-1}
DG Tau B		
This Thesis	$+9.94 \pm 4.11$	-21.00 ± 3.30
This thesis without two VLA observations	$+11.81 \pm 0.95$	-20.98 ± 1.58
Value from Rodríguez, Dzib, Loinard, Zapata, Raga, Cantó & Riera (2012)	$+3.8 \pm 1.9$	-20.6 ± 3.3
DG Tau A		
Value from this thesis	$+8.95 \pm 1.40$	-19.05 ± 1.08
Value from Rodríguez, González, Raga, Cantó, Riera, Loinard, Dzib & Zapata (2012)	$+7.5 \pm 0.9$	-19.0 ± 0.9
Value from Ducourant et al. (2005)	$+3.0 \pm 2.0$	-24.0 ± 2.0

CHAPTER 5

We have shown that DG Tau A and B have very similar proper motions, however, this alone does not determine if DG Tau A and B are a binary system. DG Tau A and B are suspected to have formed in the same star forming region, this could provide an explanation for their very similar proper motions.

DG Tau A and B are separated by approximately $55''$ (≈ 9000 AU), therefore, they do not appear to be a close binary when observed. In order to determine if DG Tau A and B are part of a binary system, follow up observations of DG Tau A and B would need to be conducted. Spectroscopic observations of both stars may determine if the observed spectral lines are being affected by the Doppler effect. This may reveal if DG Tau A and B are orbiting around a common barycentre.

Chapter 6

Conclusion and Future Work

Observations of the Young Stellar Object DG Tau B have been conducted in this thesis. Observations have been carried out at cm wavelengths using the interferometer e-MERLIN and mm wavelengths using the EVLA. We suggested an upper limit for the grain size distribution in the DG Tau B disc. We have determined the source of the cm emission detected from DG Tau B. Analysis of the proper motions of DG Tau B and the classical T-Tauri star DG Tau A have also been conducted in order to determine if they are a binary system.

6.1 SED Fitting

The flux density of DG Tau B from previous observations as well as in this thesis were used to plot a spectral energy distribution of DG Tau B. This thesis is focussed on the cold dust in the protoplanetary disc. Therefore, a modified blackbody was used to model the SED at wavelengths longer than 100 microns. The cold dust was modelled with a temperature of $T=9.6\pm 0.6\text{K}$ and a mass of $M=0.30\pm 0.03M_{\odot}$.

We have found a radio excess above the greybody spectrum. The radio excess of the SED was modelled using a power law and a spectral index of $\alpha = 1.4 \pm 0.2$.

CHAPTER 6

This is a combination of the thermal greybody ($\alpha_{greybody} = 3.0 \pm 0.1$) and free-free/synchrotron ($\alpha_{free-free/sync} = 0.3 \pm 0.2$) spectral indices. Following Draine (2006) where a spectral index of $2.0 < \alpha < 3.0$ is indicative of large dust grains and a spectral index of $-0.1 < \alpha < 1.0$ can be attributed to stellar winds and jets, we suspect that the emission detected from DG Tau B at cm wavelengths is due to synchrotron or free-free emission rather than blackbody emission.

6.2 Centimetre Observations of DG Tau B

Centimetre observations of DG Tau B were taken with the interferometer e-MERLIN at 6.48GHz (4.63cm) and 7.25GHz (4.14cm). Both observations revealed an elongated structure orientated from NW to SE. By comparing our observations to those made in Zapata et al. (2015), we hypothesis that we have detected the jet of DG Tau B with e-MERLIN rather than the disc.

Two-dimensional Gaussian models were fit to DG Tau B in each epoch in order to determine its position and the extent of its emission. DG Tau B was found to have a position of $\alpha_{J2000.0} = +04^h27^m02.574^s \pm 0.001^s$, $\delta_{J2000.0} = +26^\circ05'30.274'' \pm 0.004''$ in 2014, with a deconvolved size of $133 \times 74 \pm 27 \times 18$ mas at a position angle of $106 \pm 18^\circ$.

In 2016 DG Tau B was found to have a position of $\alpha_{J2000.0} = +04^h27^m02.576^s \pm 0.001^s$, $\delta_{J2000.0} = +26^\circ05'30.211'' \pm 0.005''$ with a deconvolved size of $153 \times 83 \pm 32 \times 11$ mas at a position angle of $130 \pm 8^\circ$.

The major axis of an elliptical Gaussian fit to DG Tau B is aligned parallel to the jet whilst the minor axis is aligned parallel to the disc. Cross cuts were made of the observations in order to determine if the emission parallel and perpendicular to the Gaussian models were resolved or not. The emission parallel to the major axis of the Gaussian model has been resolved in both the 2014 and 2016 e-MERLIN observations. However, the emission parallel to the minor axis of the Gaussian

CHAPTER 6

model is unresolved in the 2014 observations and only slightly resolved in the 2016 observations.

The 2014 and 2016 e-MERLIN observations were then combined in order to improve the signal to noise of the observations. There did not appear to be significant improvement to the signal to noise of the structure parallel to the disc when compared to the 2014 and 2016 observations separately. The signal to noise of the emission in the direction of the jet did improve in the combined observation compared to the separate observations. The emission both parallel and perpendicular to the jet of DG Tau B has been resolved in the combined observations, but more so parallel to the jet.

Therefore, we conclude that the jet of DG Tau B, rather than the protoplanetary disc, has been detected at cm wavelengths. The shallow spectral index of the radio excess of the SED, which is indicative of free-free emission, supports our conclusion. The lack of cm thermal emission from DG Tau B may indicate that this Young Stellar Object is too young to begin the formation of cm-sized dust grains.

6.3 Millimetre Observations of DG Tau B

DG Tau B has also been studied at mm wavelengths using the interferometer EVLA at 34.0GHz (8.8mm) in 2010. An elongated structure is also visible in the EVLA observations. However this lies perpendicular to the structure seen in the e-MERLIN observations. A two-dimensional Gaussian model determined the position of DG Tau B to be $\alpha_{J2000.0} = +04^h27^m02.5724^s \pm 0.0001^s$, $\delta_{J2000.0} = +26^\circ05'30.293''$ with a deconvolved size of $113.0 \times 71.4 \pm 7.0 \times 6.4$ mas with a position angle of $25.5 \pm 6.8^\circ$.

A two-dimensional elliptical Gaussian model was fit to DG Tau B with the major axis aligned parallel to the disc of DG Tau B, whilst the minor axis is aligned parallel to the jet. Analysis of the emission parallel and perpendicular to the Gaussian model revealed that the disc of DG Tau B has been resolved using the EVLA whilst the

CHAPTER 6

jet has not.

The detection of mm thermal emission, and a lack of cm thermal emission, in the direction of the DG Tau B disc may imply that mm-sized dust grains are present, but not cm-sized grains. This puts an upper limit on the grain size distribution in the disc surrounding DG Tau B. The thermal blackbody radiation from the disc of DG Tau B may simply be indicative of the dust temperature in the disc.

6.4 The relationship between DG Tau A and B

The positions of DG Tau A and B found in this thesis were used alongside literature values to determine the proper motion of each YSO. This analysis was conducted in order to determine if DG Tau A and B are a binary system.

The best fit proper motions of DG Tau B were determined to be $\mu_{\alpha_b} \cos \delta = +11.81 \pm 0.95 \text{ mas yr}^{-1}$, $\mu_{\delta_b} = -20.98 \pm 1.58 \text{ mas yr}^{-1}$. These are consistent with the calculated proper motions of DG Tau A; $\mu_{\alpha_a} \cos \delta = +8.95 \pm 1.40 \text{ mas yr}^{-1}$, $\mu_{\delta_a} = -19.05 \pm 1.08 \text{ mas yr}^{-1}$.

DG Tau A and B are thought to have formed from the same star forming regions; which may explain their similar proper motions. If they are indeed locked in a binary system they would be considered a wide binary as they are separated by $\approx 55''$ (9000AU). In order to confirm this, further observations would need to be conducted.

6.5 Future Work

There are various ways in which the work in this thesis could be extended.

Structure from DG Tau B may have been lost during the cleaning process of the 2016 e-MERLIN observation. This may explain the inconsistency between the jet angle measured in the 2016 observation and the angles measured in the 2014

CHAPTER 6

e-MERLIN, EVLA and literature observations. The data reduction of the 2016 observation could be repeated in order to determine if structure was lost during the original cleaning process. The analysis presented in this thesis could then be repeated for the newly cleaned data.

Follow up spectroscopic observations of both DG Tau A and B could also be conducted. The observed spectral lines of both stars could be compared in order to determine if they are being affected by the Doppler effect. This may reveal if DG Tau A and B are orbiting around a common barycentre.

Observations of DG Tau B using the Atacama Large Millimetre Array (ALMA) could also be conducted. This may resolve some of the structure in the disc of DG Tau B.

Bibliography

- Adams, F. C., Lada, C. J. & Shu, F. H. (1987), ‘Spectral evolution of young stellar objects’, *Astrophys. J.* **312**, 788–806.
- Ainsworth, R. E., Ray, T. P., Scaife, A. M. M., Greaves, J. S. & Beswick, R. J. (2013), ‘Subarcsecond high-sensitivity measurements of the DG Tau jet with e-MERLIN’, *Mon. Not. Roy. Astron. Soc.* **436**, L64–L68.
- AMI Consortium, Scaife, A. M. M., Buckle, J. V., Ainsworth, R. E., Davies, M., Franzen, T. M. O., Grainge, K. J. B., Hobson, M. P., Hurley-Walker, N., Lasenby, A. N., Olamaie, M., Perrott, Y. C., Pooley, G. G., Ray, T. P., Richer, J. S., Rodríguez-Gonzálvez, C., Saunders, R. D. E., Schammel, M. P., Scott, P. F., Shimwell, T., Titterton, D. & Waldram, E. (2012), ‘Radio continuum observations of Class I protostellar discs in Taurus: constraining the greybody tail at centimetre wavelengths’, *Mon. Not. Roy. Astron. Soc.* **420**, 3334–3343.
- Andre, P. (1994), Observations of protostars and protostellar stages, *in* T. Montmerle, C. Lada, I. Mirabel & J. Tran Thanh Van, eds, ‘The Cold Universe, Proceedings of the 28th Rencontre de Moriond’, Editions Frontieres.
- Andre, P., Ward-Thompson, D. & Barsony, M. (1993), ‘Submillimeter continuum observations of Rho Ophiuchi A - The candidate protostar VLA 1623 and prestellar clumps’, *Astrophys. J.* **406**, 122–141.

- Andrews, S. M. & Williams, J. P. (2005), ‘Circumstellar Dust Disks in Taurus-Auriga: The Submillimeter Perspective’, *Astrophys. J.* **631**, 1134–1160.
- Anglada, G., Tafalla, M., Carrasco-Gonzalez, C., de Gregorio-Monsalvo, I., Estrella, R., Huelamo, N., Morata, O., Osorio, M., Palau, A. & Torrelles, J. M. (2015), Protoplanetary disks, jets and the birth of their stars, *in* M. Perez-Torres, L. Verdes-Montenegro, J. Guirado, A. Alberdi, J. Martin-Pintado, R. Bachiller, D. Herranz, J. Girart, S. Migliari & J. Rodriguez-Espinosa, eds, ‘The Spanish Square Kilometre Array White Book’, ArXiv e-prints.
- Bate, M. R., Bonnell, I. A., Clarke, C. J., Lubow, S. H., Ogilvie, G. I., Pringle, J. E. & Tout, C. A. (2000), ‘Observational implications of precessing protostellar discs and jets’, *Mon. Not. Roy. Astron. Soc.* **317**, 773–781.
- Beckwith, S. V. W. & Sargent, A. I. (1991), ‘Particle emissivity in circumstellar disks’, *Astrophys. J.* **381**, 250–258.
- Beckwith, S. V. W., Sargent, A. I., Chini, R. S. & Guesten, R. (1990), ‘A survey for circumstellar disks around young stellar objects’, *Astron. J.* **99**, 924–945.
- Beitz, E., Guttler, C., Meisner, T. & Wurm, G. (2011), ‘Low-velocity Collisions of Centimeter-sized Dust Aggregates’, *Astrophys. J.* **736**, 34.
- Blum, J. & Munch, M. (1993), ‘Experimental investigations on aggregate-aggregate collisions in the early solar nebula’, *Icarus* **106**, 151.
- Blum, J. & Wurm, G. (2008), ‘The Growth Mechanisms of Macroscopic Bodies in Protoplanetary Disks’, *Ann. Rev. Astron. Astrophys.* **46**, 21–56.
- Bryden, G., Beichman, C. A., Carpenter, J. M., Rieke, G. H., Stapelfeldt, K. R., Werner, M. W., Tanner, A. M., Lawler, S. M., Wyatt, M. C., Trilling, D. E., Su,

- K. Y. L., Blaylock, M. & Stansberry, J. A. (2009), ‘Planets and Debris Disks: Results from a Spitzer/MIPS Search for Infrared Excess’, *Astrophys. J.* **705**, 1226–1236.
- Burke, B. & Graham-Smith, F. (1997), *An Introduction to Radio Astronomy*, Cambridge University Press.
- Calvet, N., D’Alessio, P., Hartmann, L., Wilner, D., Walsh, A. & Sitko, M. (2002), ‘Evidence for a Developing Gap in a 10 Myr Old Protoplanetary Disk’, *Astrophys. J.* **568**, 1008–1016.
- Calvet, N., Patino, A., Magris, G. C. & D’Alessio, P. (1991), ‘Irradiation of accretion disks around young objects. I - Near-infrared CO bands’, *Astrophys. J.* **380**, 617–630.
- Carrasco-González, C., Anglada, G., Rodríguez, L. F., Torrelles, J. M., Osorio, M. & Girart, J. M. (2008), ‘A Multiple System of Radio Sources at the Core of the L723 Multipolar Outflow’, *Astrophys. J.* **676**, 1073–1081.
- Chandler, C. (2017), Private Communication.
- Chiang, E. I. & Goldreich, P. (1997), ‘Spectral Energy Distributions of T Tauri Stars with Passive Circumstellar Disks’, *Astrophys. J.* **490**, 368–376.
- Clark, B. G. (1989), Coherence in Radio Astronomy, *in* R. A. Perley, F. R. Schwab & A. H. Bridle, eds, ‘Synthesis Imaging in Radio Astronomy’, Vol. 6 of *Astronomical Society of the Pacific Conference Series*, pp. 1–9.
- Draine, B. T. (2006), ‘On the Submillimeter Opacity of Protoplanetary Disks’, *Astrophys. J.* **636**, 1114–1120.
- Ducourant, C., Teixeira, R., Périé, J. P., Lecampion, J. F., Guibert, J. & Sartori,

- M. J. (2005), ‘Pre-main sequence star Proper Motion Catalogue’, *Astron. Astrophys.* **438**, 769–778.
- Dullemond, C. P., Hollenbach, D., Kamp, I. & D’Alessio, P. (2007), ‘Models of the Structure and Evolution of Protoplanetary Disks’, *Protostars and Planets V* pp. 555–572.
- Dunham, M. M., Vorobyov, E. I. & Arce, H. G. (2014), ‘On the reliability of protostellar disc mass measurements and the existence of fragmenting discs’, *Mon. Not. Roy. Astron. Soc.* **444**, 887–901.
- Dutrey, A., Guilloteau, S., Duvert, G., Prato, L., Simon, M., Schuster, K. & Menard, F. (1996), ‘Dust and gas distribution around T Tauri stars in Taurus-Auriga. I. Interferometric 2.7mm continuum and ^{13}CO J=1-0 observations’, *Astron. Astrophys.* **309**, 493–504.
- Eislöffel, J. & Mundt, R. (1998), ‘Imaging and Kinematic Studies of Young Stellar Object Jets in Taurus’, *Astron. J.* **115**, 1554–1575.
- Evans, M. G., Ilee, J. D., Boley, A. C., Caselli, P., Durisen, R. H., Hartquist, T. W. & Rawlings, J. M. C. (2015), ‘Gravitational instabilities in a protosolar-like disc - I. Dynamics and chemistry’, *Mon. Not. Roy. Astron. Soc.* **453**, 1147–1163.
- Evans, M. G., Ilee, J. D., Hartquist, T. W., Caselli, P., Szűcs, L., Purser, S. J. D., Boley, A. C., Durisen, R. H. & Rawlings, J. M. C. (2017), ‘Gravitational instabilities in a protosolar-like disc - II. Continuum emission and mass estimates’, *Mon. Not. Roy. Astron. Soc.* **470**, 1828–1847.
- Garrington, S. T., Anderson, B., Baines, C., Battilana, J. A., Bentley, M. N., Brown, D., Burgess, P., Diamond, P. J., Kitching, G. J., McCool, R., Muxlow, T. W., Noble, R. G., Roddis, N., Spencer, R. E. & Thomasson, P. (2004), e-MERLIN, *in*

- J. M. Oschmann, Jr., ed., ‘Ground-based Telescopes’, Vol. 5489 of *Proceedings of the SPIE*, pp. 332–343.
- Gramajo, L. V., Whitney, B. A., Gómez, M. & Robitaille, T. P. (2010), ‘Combined Analysis of Images and Spectral Energy Distributions of Taurus Protostars’, *Astron. J.* **139**, 2504–2524.
- Greaves, J. (2017), Private Communication.
- Guilloteau, S., Dutrey, A., Piétu, V. & Boehler, Y. (2011), ‘A dual-frequency sub-arcsecond study of proto-planetary disks at mm wavelengths: first evidence for radial variations of the dust properties’, *Astron. Astrophys.* **529**, A105.
- Haro, G. (1952), ‘Herbig’s Nebulous Objects Near NGC 1999.’, *Astrophys. J.* **115**, 572.
- Hartmann, L. (1998), *Accretion Processes in Star Formation*, Cambridge University Press.
- Hartmann, L., Calvet, N., Gullbring, E. & D’Alessio, P. (1998), ‘Accretion and the Evolution of T Tauri Disks’, *Astrophys. J.* **495**, 385–400.
- Hartmann, L., Megeath, S. T., Allen, L., Luhman, K., Calvet, N., D’Alessio, P., Franco-Hernandez, R. & Fazio, G. (2005), ‘IRAC Observations of Taurus Pre-Main-Sequence Stars’, *Astrophys. J.* **629**, 881–896.
- Herbig, G. H. (1951), ‘The Spectra of Two Nebulous Objects Near NGC 1999.’, *Astrophys. J.* **113**, 697–699.
- Hildebrand, R. H. (1983), ‘The Determination of Cloud Masses and Dust Characteristics from Submillimetre Thermal Emission’, *Qua. J. Roy. Astron. Soc.* **24**, 267.

- Högbom, J. A. (1974), ‘Aperture Synthesis with a Non-Regular Distribution of Interferometer Baselines’, *Astron. Astrophys. Suppl.* **15**, 417.
- Hollenbach, D., Johnstone, D., Lizano, S. & Shu, F. (1994), ‘Photoevaporation of disks around massive stars and application to ultracompact H II regions’, *Astrophys. J.* **428**, 654–669.
- Isella, A., Carpenter, J. M. & Sargent, A. I. (2010), ‘Investigating Planet Formation in Circumstellar Disks: CARMA Observations of Ry Tau and Dg Tau’, *Astrophys. J.* **714**, 1746–1761.
- Jones, B. F. & Cohen, M. (1986), ‘Observations of jets from low-luminosity stars - DG Tauri B’, *Astrophys. J. Letters* **311**, L23–L26.
- Kenyon, S. J. & Hartmann, L. (1987), ‘Spectral energy distributions of T Tauri stars - Disk flaring and limits on accretion’, *Astrophys. J.* **323**, 714–733.
- Kitamura, Y., Kawabe, R. & Saito, M. (1996), ‘Imaging of the Compact Dust Disk around DG Tauri with 1 Resolution’, *Astrophys. J. Letters* **465**, L137.
- Lada, C. J. (1985), ‘Cold outflows, energetic winds, and enigmatic jets around young stellar objects’, *Ann. Rev. Astron., Astrophys.* **23**, 267–317.
- Lada, C. J. (1987), Star formation - From OB associations to protostars, in M. Peimbert & J. Jugaku, eds, ‘Star Forming Regions’, Vol. 115 of *IAU Symposium*, pp. 1–17.
- Lommen, D., Maddison, S. T., Wright, C. M., van Dishoeck, E. F., Wilner, D. J. & Bourke, T. L. (2009), ‘Large grains in discs around young stars: ATCA observations of WW Chamaeleontis, RU Lupi, and CS Chamaeleontis’, *Astron. Astrophys.* **495**, 869–879.

- López, R., Acosta-Pulido, J. A., Estalella, R., Gómez, G. & García-Lorenzo, B. (2015), ‘3D kinematics of the near-IR HH 223 outflow in L723’, *Mon. Not. Roy. Astron. Soc.* **447**, 2588–2602.
- López, R., Estalella, R., Gómez, G. & Riera, A. (2006), ‘Optical imaging of L723: the structure of HH 223’, *Astron. Astrophys.* **454**, 233–238.
- Luhman, K. L., Allen, P. R., Espaillat, C., Hartmann, L. & Calvet, N. (2010), ‘The Disk Population of the Taurus Star-Forming Region’, *Astrophys. J. Supple.* **186**, 111–174.
- Malbet, F. & Bertout, C. (1991), ‘The vertical structure of T Tauri accretion disks. I - Heating by the central star’, *Astrophys. J.* **383**, 814–819.
- McGroarty, F. & Ray, T. P. (2004), ‘Classical T Tauri stars as sources of parsec-scale optical outflows’, *Astron. Astrophys.* **420**, 975–986.
- McGroarty, F., Ray, T. P. & Froebrich, D. (2007), ‘Proper motion studies of outflows from Classical T Tauri stars’, *Astron. Astrophys.* **467**, 1197–1207.
- Mendoza V., E. E. (1968), ‘Infrared Excesses in T Tauri Stars and Related Objects’, *Astrophys. J.* **151**, 977.
- Mitchell, G. F., Hasegawa, T. I., Dent, W. R. F. & Matthews, H. E. (1994), ‘A molecular outflow driven by an optical jet’, *Astrophys. J. Letters* **436**, L177–L180.
- Mitchell, G. F., Sargent, A. I. & Mannings, V. (1997), ‘DG Tauri B: The Interaction of an Atomic Jet with Ambient Molecular Gas’, *Astrophys. J. Letters* **483**, L127–L130.
- Mundt, R. & Fried, J. W. (1983), ‘Jets from young stars’, *Astrophys. J. Letters* **274**, L83–L86.

- Mundt, R., Ray, T. P. & Raga, A. C. (1991), ‘Collimation of Stellar Jets - Constraints from the Observed Spatial Structure - Part Two - Observational Results’, *Astron. Astrophys.* **252**, 740.
- Olson, F. M. (1975), ‘Thermal bremsstrahlung radiospectra for inhomogeneous objects, with an application to MWC 349.’, *Astron. Astrophys.* **39**, 217–223.
- Padgett, D. L., Brandner, W., Stapelfeldt, K. R., Strom, S. E., Terebey, S. & Koerner, D. (1999), ‘Hubble Space Telescope / NICMOS Imaging of Disks and Envelopes around Very Young Stars’, *Astron. J.* **117**, 1490–1504.
- Panagia, N. & Felli, M. (1975), ‘The spectrum of the free-free radiation from extended envelopes’, *Astron. Astrophys.* **39**, 1–5.
- Perley, R. A., Chandler, C. J., Butler, B. J. & Wrobel, J. M. (2011), ‘The Expanded Very Large Array: A New Telescope for New Science’, *Astrophys. J. Letters* **739**, L1.
- Podio, L., Kamp, I., Flower, D., Howard, C., Sandell, G., Mora, A., Aresu, G., Brittain, S., Dent, W. R. F., Pinte, C. & White, G. J. (2012), ‘Herschel/PACS observations of young sources in Taurus: the far-infrared counterpart of optical jets’, *Astron. Astrophys.* **545**, A44.
- Pollack, J. B., Hubickyj, O., Bodenheimer, P., Lissauer, J. J., Podolak, M. & Greenzweig, Y. (1996), ‘Formation of the Giant Planets by Concurrent Accretion of Solids and Gas’, *Icarus* **124**, 62–85.
- Pudritz, R. E. & Norman, C. A. (1983), ‘Centrifugally driven winds from contracting molecular disks’, *Astrophys. J.* **274**, 677–697.
- Pudritz, R. E. & Norman, C. A. (1986), ‘Bipolar hydromagnetic winds from disks around protostellar objects’, *Astrophys. J.* **301**, 571–586.

- Rayleigh, L. (1879), ‘Investigations in optics with special reference to spectroscopy’, *Philosophical Magazine* **8**, 261–274.
- Reynolds, S. P. (1986), ‘Continuum spectra of collimated, ionized stellar winds’, *Astrophys. J.* **304**, 713–720.
- Robitaille, T. P., Whitney, B. A., Indebetouw, R. & Wood, K. (2007), ‘Interpreting Spectral Energy Distributions from Young Stellar Objects. II. Fitting Observed SEDs Using a Large Grid of Precomputed Models’, *Astrophys. J. Supple.* **169**, 328–352.
- Robitaille, T. P., Whitney, B. A., Indebetouw, R., Wood, K. & Denzmore, P. (2006), ‘Interpreting Spectral Energy Distributions from Young Stellar Objects. I. A Grid of 200,000 YSO Model SEDs’, *Astrophys. J. Supple.* **167**, 256–285.
- Rodmann, J., Henning, T., Chandler, C. J., Mundy, L. G. & Wilner, D. J. (2006), ‘Large dust particles in disks around T Tauri stars’, *Astron. Astrophys.* **446**, 211–221.
- Rodríguez, L. F., Dzib, S. A., Loinard, L., Zapata, L. A., Raga, A. C., Cantó, J. & Riera, A. (2012), ‘Radio and Optical Observations of DG Tau B’, *Revista Mexicana de Astronomía y Astrofísica* **48**, 243–249.
- Rodríguez, L. F., González, R. F., Raga, A. C., Cantó, J., Riera, A., Loinard, L., Dzib, S. A. & Zapata, L. A. (2012), ‘Radio continuum emission from knots in the DG Tauri jet’, *Astron. Astrophys.* **537**, A123.
- Rohlfs, K. & Wilson, T. (2000), *Tools of Radio Astronomy*, Springer.
- Schneider, P. C., Eisloffel, J., Güdel, M., Günther, H. M., Herczeg, G., Robrade, J. & Schmitt, J. H. M. M. (2013), ‘HST far-ultraviolet imaging of DG Tauri. Fluorescent molecular hydrogen emission from the wide opening-angle outflow’, *Astron. Astrophys.* **557**, A110.

- Schwartz, R. D. (1975), ‘T Tauri Nebulae and Herbig-Haro Nebulae - Evidence for excitation by a strong stellar wind’, *Astrophys. J.* **195**, 631–642.
- Snell, R. L., Loren, R. B. & Plambeck, R. L. (1980), ‘Observations of CO in L1551 - Evidence for stellar wind driven shocks’, *Astrophys. J.* **239**, L17–L22.
- Stapelfeldt, K., Burrows, C. J., Krist, J. E. & WFPC2 Science Team (1997), Hubble Space Telescope Imaging of the Disks and Jets of Taurus Young Stellar Objects, *in* B. Reipurth & C. Bertout, eds, ‘Herbig-Haro Flows and the Birth of Stars’, Vol. 182 of *IAU Symposium*, pp. 355–364.
- Terquem, C., Eisloffel, J., Papaloizou, J. C. B. & Nelson, R. P. (1999), ‘Precession of Collimated Outflows from Young Stellar Objects’, *Astrophys. J. Letters* **512**, L131–L134.
- Testi, L., Birnstiel, T., Ricci, L., Andrews, S., Blum, J., Carpenter, J., Dominik, C., Natta, A., Williams, J. & Wilner, D. (2014), Dust evolution in protoplanetary disks, *in* H. Beuther, R. Klessen, C. Dullemond & T. Hennings, eds, ‘Protostars and Planets VI’, University of Arizona Press, pp. 339–361.
- Testi, L., Natta, A., Shepherd, D. S. & Wilner, D. J. (2003), ‘Large grains in the disk of CQ Tau’, *Astron. Astrophys.* **403**, 323–328.
- Thompson, R. A. (1989), The Interferometer in Practice, *in* R. A. Perley, F. R. Schwab & A. H. Bridle, eds, ‘Synthesis Imaging in Radio Astronomy’, Vol. 6 of *Astronomical Society of the Pacific Conference Series*, pp. 11–34.
- Torres, R. M., Loinard, L., Mioduszewski, A. J., Boden, A. F., Franco-Hernández, R., Vlemmings, W. H. T. & Rodríguez, L. F. (2012), ‘VLBA Determination of the Distance to nearby Star-forming Regions. V. Dynamical Mass, Distance, and Radio Structure of V773 Tau A’, *Astrophys. J.* **747**, 18.

- Torres, R. M., Loinard, L., Mioduszewski, A. J. & Rodríguez, L. F. (2007), ‘VLBA Determination of the Distance to Nearby Star-forming Regions. II. Hubble 4 and HDE 283572 in Taurus’, *Astrophys. J.* **671**, 1813–1819.
- Torres, R. M., Loinard, L., Mioduszewski, A. J. & Rodríguez, L. F. (2009), ‘VLBA Determination of the Distance to Nearby Star-Forming Regions. III. HP TAU/G2 and the Three-Dimensional Structure of Taurus’, *Astrophys. J.* **698**, 242–249.
- van Cittert, P. H. (1934), ‘Die Wahrscheinliche Schwingungsverteilung in Einer von Einer Lichtquelle Direkt Oder Mittels Einer Linse Beleuchteten Ebene’, *Physica* **1**, 201–210.
- Walker, C. K., Lada, C. J., Young, E. T. & Margulis, M. (1988), ‘An unusual outflow around IRAS 16293-2422’, *Astrophys. J.* **332**, 335–345.
- Ward-Thompson, D. & Whitworth, A. P. (2011), *An Introduction to Star Formation*, Cambridge University Press.
- Watson, D. M., Kemper, F., Calvet, N., Keller, L. D., Furlan, E., Hartmann, L., Forrest, W. J., Chen, C. H., Uchida, K. I., Green, J. D., Sargent, B., Sloan, G. C., Herter, T. L., Brandl, B. R., Houck, J. R., Najita, J., D’Alessio, P., Myers, P. C., Barry, D. J., Hall, P. & Morris, P. W. (2004), ‘Mid-infrared Spectra of Class I Protostars in Taurus’, *Astrophys. J. Supple.* **154**, 391–395.
- Weidenschilling, S. (1977), ‘Aerodynamics of solid bodies in the solar nebula’, *Mon. Not. Roy. Astron. Soc.* **180**, 57–70.
- Wien, W. (1897), ‘On the division of energy in the emission-spectrum of a black body’, *Philosophical Magazine* **43**, 214–220.
- Wilner, D. J., D’Alessio, P., Calvet, N., Claussen, M. J. & Hartmann, L. (2005), ‘Toward Planetesimals in the Disk around TW Hydrae: 3.5 Centimeter Dust Emission’, *Astrophys. J. Letters* **626**, L109–L112.

- Windmark, F., Birnstiel, T., Guttler, C., Blum, J., Dullemond, C. & Henning, T. (2012), ‘Planetesimal formation by sweep-up: how the bouncing barrier can be beneficial to growth’, *Astron. Astrophys.* **540**, A73.
- Wolszczan, A. & Frail, D. A. (1992), ‘A Planetary system around the millisecond pulsar PSR1257+12’, *Nature* **355**, 145–147.
- Wright, A. E. & Barlow, M. J. (1975), ‘The radio and infrared spectrum of early-type stars undergoing mass loss’, *Mon. Not. Roy. Astron. Soc.* **170**, 41–51.
- Wurm, G., Paraskov, G. & Krauss, O. (2005), ‘Growth of planetesimals by impacts at 25 m/s’, *Icarus* **178**, 253–263.
- Zapata, L. A., Lizano, S., Rodríguez, L. F., Ho, P. T. P., Loinard, L., Fernández-López, M. & Tafuya, D. (2015), ‘Kinematics of the Outflow from the Young Star DG Tau B: Rotation in the Vicinities of an Optical Jet’, *Astrophys. J.* **798**, 131.
- Zernike, F. (1938), ‘The concept of degree of coherence and its application to optical problems’, *Physica* **5**, 785–795.